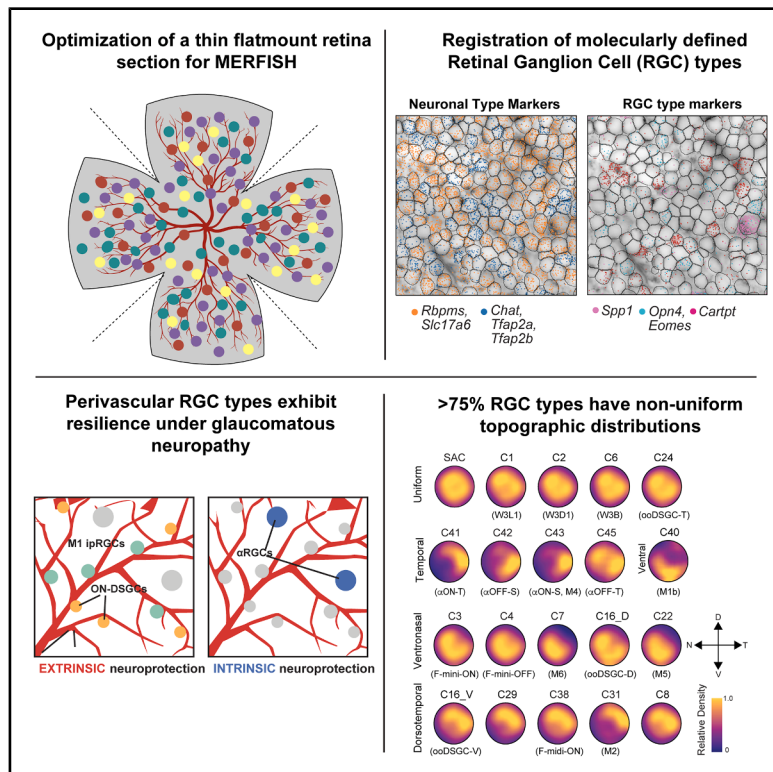


# Molecular and spatial analysis of ganglion cells on retinal flatmounts identifies perivascular neurons resilient to glaucoma

## Graphical abstract



## Authors

Kushal Nimkar, Nicole Y. Tsai,  
Mengya Zhao, ..., Benjamin Sivyer,  
Karthik Shekhar, Xin Duan

## Correspondence

kshekhar@berkeley.edu (K.S.),  
xin.duan@ucsf.edu (X.D.)

## In brief

Nimkar and colleagues present a flatmount spatial transcriptomics platform for mapping the distribution of retinal ganglion cell (RGC) types. The analysis uncovers systematic topographic biases among RGC types and identifies perivascular RGC types surviving preferentially after experimental glaucoma. The results highlight neuroprotective roles of perivascular niche in the retina.

## Highlights

- Spatial transcriptomic analysis of retinal ganglion cells (RGCs) in flat-mounts
- ~75% of molecularly defined RGC types exhibit biased topographic distributions
- Seven RGC types are enriched in the perivascular niche
- Perivascularity confers enhanced neuroprotection under glaucomatous conditions

## Article

# Molecular and spatial analysis of ganglion cells on retinal flatmounts identifies perivascular neurons resilient to glaucoma

Kushal Nimkar,<sup>1,10</sup> Nicole Y. Tsai,<sup>2,10</sup> Mengya Zhao,<sup>2,10</sup> Yujuan Yi,<sup>2</sup> Matthew R. Lum,<sup>2</sup> Tavita R. Garrett,<sup>3</sup> Yixiao Wang,<sup>2</sup> Kenichi Toma,<sup>2</sup> Franklin Caval-Holme,<sup>4</sup> Nikhil Reddy,<sup>1</sup> Aliza T. Ehrlich,<sup>5</sup> Arnold R. Kriegstein,<sup>6</sup> Michael Tri H. Do,<sup>4</sup> Yang Hu,<sup>7</sup> Benjamin Sivyer,<sup>3</sup> Karthik Shekhar,<sup>1,8,11,\*</sup> and Xin Duan<sup>2,9,11,12,\*</sup>

<sup>1</sup>Department of Chemical and Biomolecular Engineering, University of California, Berkeley, Berkeley, CA, USA

<sup>2</sup>Department of Ophthalmology, School of Medicine, University of California, San Francisco, San Francisco, CA, USA

<sup>3</sup>Casey Eye Institute, Oregon Health and Science University, Portland, OR, USA

<sup>4</sup>Department of Neurology, F.M. Kirby Neurobiology Center, Boston Children's Hospital, Harvard Medical School, Boston, MA, USA

<sup>5</sup>Department of Psychiatry and Behavioral Sciences, University of California, San Francisco, San Francisco, CA, USA

<sup>6</sup>Department of Neurology, The Eli and Edythe Broad Center of Regeneration Medicine and Stem Cell Research, University of California, San Francisco, San Francisco, CA, USA

<sup>7</sup>Department of Ophthalmology, Spencer Center for Vision Research, Byers Eye Institute at Stanford University School of Medicine, Palo Alto, CA, USA

<sup>8</sup>Helen Wills Neuroscience Institute, Vision Sciences Graduate Program, Center for Computational Biology, Biophysics Graduate Group, University of California, Berkeley, Berkeley, CA, USA

<sup>9</sup>Department of Physiology, Kavli Institute for Fundamental Neuroscience, University of California, San Francisco, San Francisco, CA, USA

<sup>10</sup>These authors contributed equally

<sup>11</sup>These authors contributed equally

<sup>12</sup>Lead contact

\*Correspondence: [kshekhar@berkeley.edu](mailto:kshekhar@berkeley.edu) (K.S.), [xin.duan@ucsf.edu](mailto:xin.duan@ucsf.edu) (X.D.)

<https://doi.org/10.1016/j.neuron.2025.07.025>

## SUMMARY

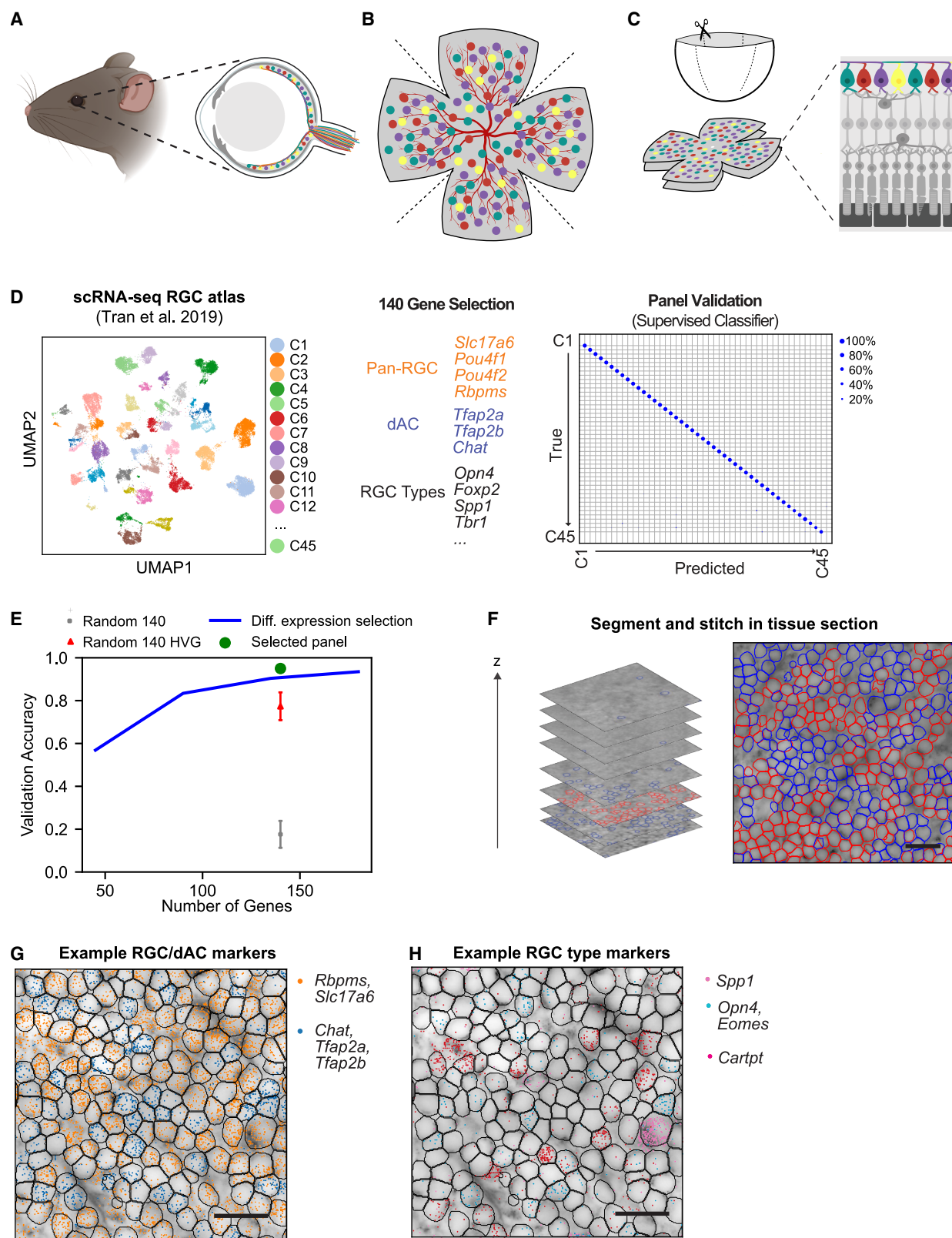
Recent transcriptomic studies have categorized mouse retinal ganglion cells (RGCs) into 45 types; however, little is known about their spatial distributions on the two-dimensional retinal surface and how their local microenvironments impact their functions. Here, we optimized a workflow combining imaging-based spatial transcriptomics (multiplexed-error robust fluorescent *in situ* hybridization [MERFISH]) and immunostaining on retinal flatmounts. We computationally registered the somata distributions of all RGCs and found that 34/45 molecularly defined types exhibited non-uniform distributions. We analyzed local neighborhoods for each cell and identified seven RGC types enriched in the perivascular niche, including direction-selective RGC (DSGC) and intrinsically photosensitive RGC (ipRGC) types. We further examined an experimental glaucoma model and found that surviving RGCs are enriched in the perivascular niche. Perivascular DSGCs and M1 ipRGCs were especially resilient, suggesting that proximity to vasculatures confers mTOR-independent, cell-extrinsic neuroprotection. Together, our work provides a comprehensive spatial atlas of RGC types and links their microenvironment to differential vulnerability in neurodegeneration.

## INTRODUCTION

Cataloging neuronal types, defining their spatial organization, and mapping neuron-neuron connectivity are essential steps for understanding the assembly and function of neural circuits.<sup>1,2</sup> The mammalian retina is an ideal model system for these studies due to its compact structure, experimental accessibility, and complex neural network, comprising multiple neuronal types.<sup>3,4</sup> Over decades of research, the mouse retina has been found to contain ~130 distinct neuronal types,<sup>5,6</sup> organized across three somatic layers.<sup>7</sup> The innermost layer, known as the ganglion cell

layer (GCL), houses the somata of retinal ganglion cells (RGCs), which are glutamatergic projection neurons. RGCs are the retina's sole output neurons, and their axons communicate visual information to the rest of the brain via the optic nerve (Figures 1A and 1B). Investigating the neurobiology of RGCs is crucial for advancing approaches to restore vision in cases of neurological injuries or ophthalmological diseases.

The RGC class comprises diverse neuronal types, most of which respond selectively to specific visual features, such as motion, orientation, or edges, channeling visual signals into multiple parallel information streams.<sup>8</sup> Recent studies have classified ~45



(legend on next page)

RGC types in mice based on molecular profiles and demonstrated their alignment with dendritic morphologies and visual responses.<sup>9–13</sup> Advances in mouse transgenics<sup>14–18</sup> and single-cell RNA sequencing (scRNA-seq)<sup>12,13</sup> have furnished markers for selectively labeling and manipulating specific RGC types. Experiments leveraging these molecular or genetic markers have enabled the mapping of synaptic connectivity within the retina and onto retinorecipient regions.<sup>15,19–21</sup> Crucially, these markers have served as a basis for unifying classification schemes.<sup>10–12</sup> Furthermore, the ability to distinguish RGC types based on their molecular profiles has also been helpful in studying their development,<sup>22,23</sup> evolutionary conservation,<sup>24</sup> and type-specific differences in responses to optic nerve injury and neurodegenerative insults.<sup>12,25–29</sup>

Although RGC classification is nearly complete in mice and quite advanced in several other species,<sup>24</sup> questions persist regarding the spatial distribution of different RGC types across the retinal surface and potential variations in their local microenvironments within the retina. Additionally, for most RGC types, it remains unclear whether their inter-somal spacing follows a non-random pattern—a characteristic known as “mosaicism” that has been documented in several retinal cell types, including some RGC types.<sup>30,31</sup> Conventional scRNA-seq techniques discard spatial information due to the requirement of enzymatic dissociation of the tissue. Recently, the application of serial section electron microscopy (EM) on intact blocks of the retina has provided detailed anatomical data for RGC types, including soma distributions and dendritic architecture.<sup>32,33</sup> However, this technique has limited throughput (~1 mm<sup>2</sup> per sample), covering only ~5% of the retinal surface. On the other hand, transgenic markers and immunohistochemical labeling<sup>34–36</sup> have examined full spatial distributions of select RGC subsets, but these approaches are limited by multiplexing constraints and potential variability from transgene positioning effects.<sup>37</sup> These technical barriers underscore the need for approaches to profile RGC diversity with spatial information over the entire retinal surface.

To map the spatial organization of RGC types across the retina, we developed a technical platform that integrates spatial transcriptomics with immunohistochemical labeling on flat-

mount retinal sections. Through computational analyses, we mapped the spatial distributions of all transcriptomically defined RGC types across the entire retinal surface. Globally, many RGC types exhibit biased distributions of somas along the dorsal-ventral (D/V) or nasal-temporal axes. Locally, nearest-neighbor statistics, benchmarked against randomized simulations that respect cell density, soma location and size, show varying degrees of regularity among RGC types.

Spatial order among RGC somas is but one facet of local organization. A separate analysis of soma-vessel distances uncovered seven RGC types that are frequently found in proximity to retinal blood vessels, including members of the intrinsically photosensitive RGC (ipRGC) and direction-selective ganglion cell (DSGC) subclasses. We validated multiplexed-error robust fluorescent *in situ* hybridization (MERFISH)-based predictions of perivascular enrichment in transgenic mouse lines and observed the same microscopic anatomical relationship in human tissue. Functionally, the perivascular niche promotes neuroprotection: under elevated intraocular pressure (IOP) simulating glaucomatous conditions, RGCs located near vessels, especially the ipRGC and DSGC perivascular types, survived preferentially. While the full mechanistic details remain to be uncovered, our data suggest that these cells rely on an mTOR-independent neuroprotective mechanism deployed in αRGCs.<sup>25</sup> Taken together, by combining spatial mapping, genetic labeling, and disease models, we demonstrate that proximity to the vasculature confers an extrinsic neuroprotective advantage to specific RGC types susceptible to optic neuropathy.

## RESULTS

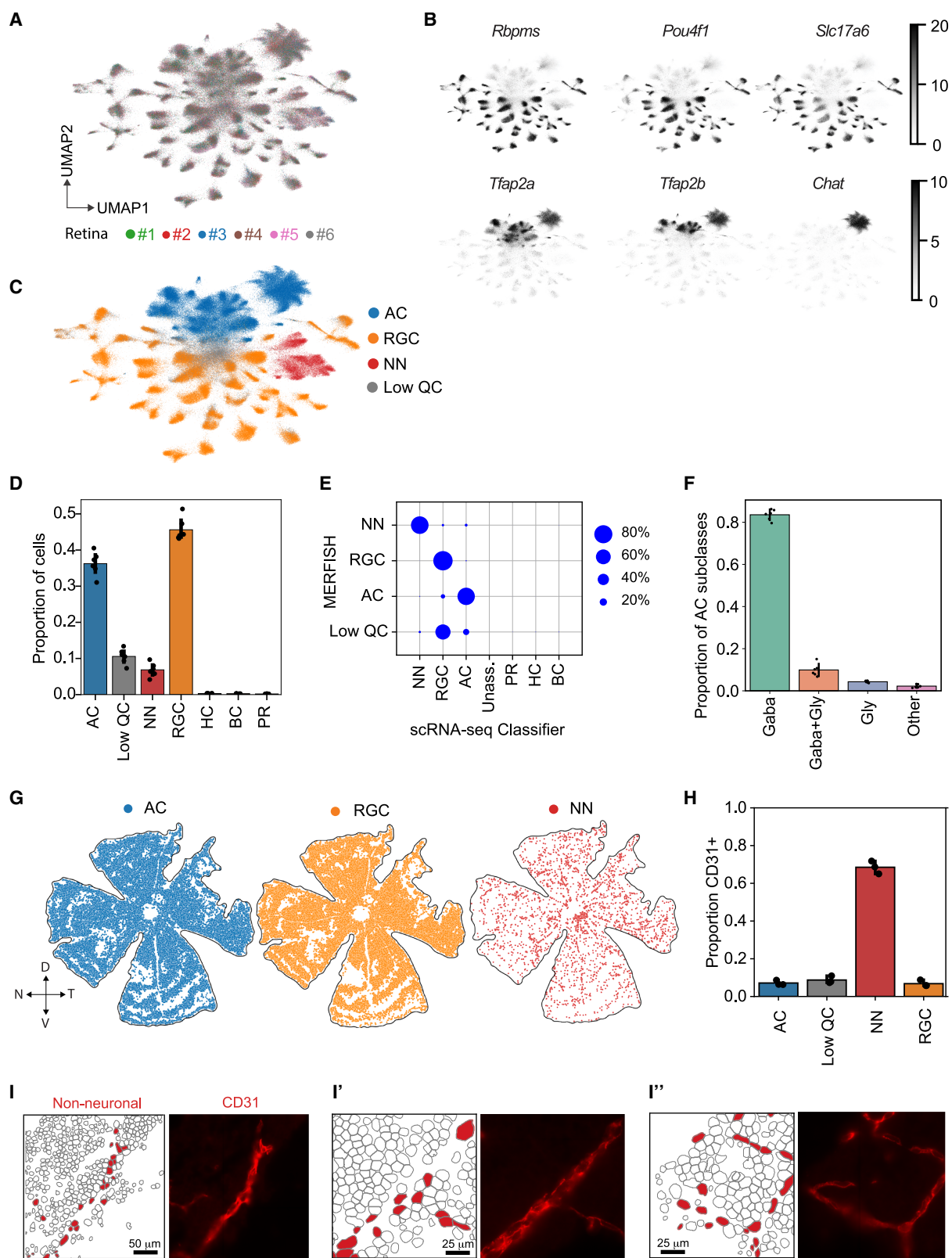
### Spatial transcriptomic imaging of retinal flatmount sections

The mouse GCL, an ~20-μm-thick monolayer, contains the somata of RGCs, displaced amacrine cells (dACs), and non-neuronal cells (NNs), such as astrocytes, endothelial cells, pericytes, and microglia. Endothelial cells, pericytes, and other NNs are assembled into the superficial layer (SL) of the retinal vasculature within the same space, spanning the

#### Figure 1. Spatial transcriptomics of the GCL in retinal flatmount sections

- (A) Illustration of mouse retina showing RGC types (colors) in the GCL.
- (B) Schematic of a GCL flatmount showing RGCs, dACs, and NNs.
- (C) The dissected retina is flattened on filter paper via relieving cuts and cryo-sectioned into ~12-μm-thick sections.
- (D) Uniform manifold approximation and projection (UMAP) visualization of RGC diversity based on scRNA-seq atlas, MERFISH gene panel consisting of 140 genes optimized for RGC classification, and confusion matrix showing the performance of an XGBoost classifier trained on these genes, and evaluated on a test set of RGCs.
- (E) Validation accuracies of the XGBoost classifier trained on various gene selections. The validation of the 140-gene panel was compared with a 140-gene panel from random subsets of 2,000 highly variable genes (HVGs). Varying numbers of genes (45, 90, 135, and 180) were selected by picking differentially expressed genes from each RGC cluster. Error bar: ±1 SD ( $n = 10$  random gene sets).
- (F) Cellpose 2.0 is applied to identify cell somata from optical sections (left), stitched together for the final segmentation (right). Red denotes cells identified in the third optical section, while blue denotes additional cells identified in consecutive sections. A 2D projection is created by consecutively adding new somata to the projection without any lateral overlap (STAR Methods).
- (G) Transcripts are visualized with the segmentation masks. Dots correspond to unique transcripts. Transcript colors correspond to marker genes for RGCs (*Rbpms*, *Slc17a6*; orange) and dACs (*Chat*, *Tfap2a*, *Tfap2b*; blue).
- (H) Transcripts are visualized for RGC subsets: αRGCs (*Spp1*), ipRGCs (*Opn4* and *Eomes*), ooDSGCs (*Cartpt*). Scale bars (F–H), 25 μm.

See also Figure S1 and Table S1.



(legend on next page)

two-dimensional (2D) surface of the retina (**Figures 1A** and **1B**). As RGCs form a flat layer of neurons in the GCL, the flatmount preparations provide comprehensive access to them. We developed an integrated experimental and computational workflow to visualize RGC diversity across the entire retina.

Our method is based on MERFISH, an imaging-based spatial transcriptomics approach<sup>38,39</sup> that visualizes individual transcripts at  $\sim 1\text{ }\mu\text{m}$  resolution (**STAR Methods**). Since MERFISH requires thin tissue sections, we optimized a protocol to obtain a series of 12- $\mu\text{m}$ -thick flatmount sections to cover the entire GCL *en face* (**Figure 1C**). We performed MERFISH imaging on these sections, targeting 140 genes optimized for classifying RGC types based on the transcriptomic profiles from our established scRNA-seq dataset<sup>12</sup> (**Figure 1D**; **Table S1**). Although the 140-gene panel covers only a small fraction of the transcriptome, simulations using the scRNA-seq atlas verified that these 140 genes reliably distinguish all 45 RGC types, with  $\sim 94\%$  precision and  $\sim 91\%$  recall (**Figures 1D**, **1E**, and **S1A–S1C**; **STAR Methods**).

A single retina yielded four to five consecutive sections, which were imaged using a standardized MERFISH imaging protocol. Cell somata within each section were segmented using a neural network model based on a cell body stain (**Figures 1F** and **S1D**; **STAR Methods**). The neural network model was based on Cellpose 2.0<sup>40</sup> but customized for our dataset through extensive training on manually curated and annotated images (**STAR Methods**). Transcripts detected in the MERFISH images were assigned to the segmented somata, yielding an mRNA profile for every cell (**Figures 1G** and **1H**). To reconstruct the entire GCL in 2D, we used a nasal-edge incision as a common landmark.<sup>41</sup> Rigid rotations and translations aligned the sections, while the same landmark allowed us to register the orientations of different retinas (**Figures S1E** and **S1F**). From the aligned data, we computed a cell-by-gene expression matrix (GEM) for each retina for downstream clustering analyses and visualization. On average, we captured  $\sim 62,000 \pm 9,800$  cells per retina, assigning each cell an  $(x, y)$  spatial coordinate within the retinal surface (**Figures S1F–S1H**).

### Separation of major cell classes in the GCL

Initial clustering of the data from all six biological replicates separated cells by their class identity (**Figures 2A–2C**; **STAR**

**Methods**). Approximately 93% of captured cells were neurons, while 7% were NNs (**Figures 2C** and **2D**). Among neurons, 89% were reliably assigned based on their expression of marker genes to the two major classes known to populate the GCL: 49% were RGCs ( $28,208 \pm 3,682$  per retina), and 39% were dACs ( $22,730 \pm 4,814$  per retina) (**Figures 2D** and **S1I**). The relative proportion of RGCs among GCL neurons ( $\sim 49\%$ ) aligns favorably with prior estimates via axon counting ( $\sim 44\%$ ).<sup>42</sup> Moreover, these estimates suggest that our method captures approximately 63% of RGCs in the GCL per retina.<sup>42</sup> The remaining 12% of neurons formed a single ambiguous cluster of low-quality cells (**Figures 2D** and **S1J**). These cells were excluded from downstream analyses. To validate our manual assignments, we used a tree-based classifier<sup>43</sup> trained on multiple scRNA-seq atlases representing major retinal cell classes (**Figure S1K**; **STAR Methods**).<sup>12,44,45</sup> The classifier confirmed our assignments of RGCs, dACs, and NNs based on the expression of marker genes. It also verified the absence of bipolar cells (BCs), photoreceptors (PRs), and horizontal cells (HCs), which are retinal neuronal classes not found in the GCL under normal conditions (**Figure 2E**).

dACs are axon-less neurons in the GCL composed of several distinct types.<sup>45,46</sup> Consistent with their known neurotransmitter profile,  $\sim 85\%$  of dACs in our dataset were classified as GABAergic (**Figure 2F**). Notably,  $32\% \pm 3\%$  of dACs expressed *Chat*, the gene encoding choline acetyltransferase, identifying them as On starburst amacrine cells (On-SACs), the most abundant dAC type<sup>47</sup> (**Figure 2B**). On-SACs innervate DSGCs, including both On-Off DSGCs and On-DSGCs.<sup>48,49</sup>

NNs comprised  $4,206 \pm 942$  cells per retina. While our RGC-focused gene panel precluded finer subtyping of these NNs, their spatial distribution was distinct from that of RGCs and dACs and could be used to trace blood vessels in the GCL (**Figure 2G**), a finding consistent with the well-known association of endothelial cells, pericytes, and astrocytes with the vasculature.<sup>50</sup> To confirm the identity of these vessels, we modified our MERFISH protocol to co-detect immunohistochemical signals along with RNA transcripts and cell segmentation (**STAR Methods**). Specifically, we targeted CD31, an endothelial cell marker, to confirm the presence of blood vessels predicted computationally (**Figures 2H** and **2I**). Moreover,  $\sim 70\%$  of NNs in our dataset are CD31<sup>+</sup>, identifying them as endothelial cells. Having established the

### Figure 2. MERFISH-based categorization of RGCs, dACs, and NNs in 2D flatmounts

- (A) 2D visualization of the MERFISH datasets. Cells are colored by their sample of origin ( $n = 6$ ).
- (B) Cells shaded by marker gene expression level. The top row panels correspond to RGC markers *Rbpms*, *Pou4f1*, and *Slc17a6*. Bottom row panels correspond to amacrine cell (AC) markers *Tfap2a*, *Tfap2b*, and *Chat*. *Chat* marks On-SACs.
- (C) Cells colored by their class of origin. RGCs and dACs are colored orange and blue, respectively, based on (B). NNs were identified using the XGBoost classifier. Low-quality cells (11%) are shown in gray.
- (D) Quantification of RGC, AC, and NN proportions across replicates (dots). Error bar: mean  $\pm$  SD ( $n = 6$ ).
- (E) Confusion matrix comparing cell class assignments based on marker genes and XGBoost classification. Each row is normalized to sum to 100%.
- (F) Composition of dAC neurotransmitter profiles, showing that GABAergic ACs (Gaba) predominate glycinergic ACs (Gly).
- (G) Example retina separately displaying the locations of RGCs (orange), ACs (blue), and the NNs (red).
- (H) Proportions for each cell class categorized as CD31<sup>+</sup> in MERFISH samples confirm the validity of using NNs to trace blood vessels (mean  $\pm$  SD;  $n = 6$ ).
- (I) Three regions highlighting blood vessels traced using MERFISH. The left panel highlights NNs (red) among segmented cells, and the right panel shows CD31 immunostaining.

See also **Figure S1** and **Table S1**.

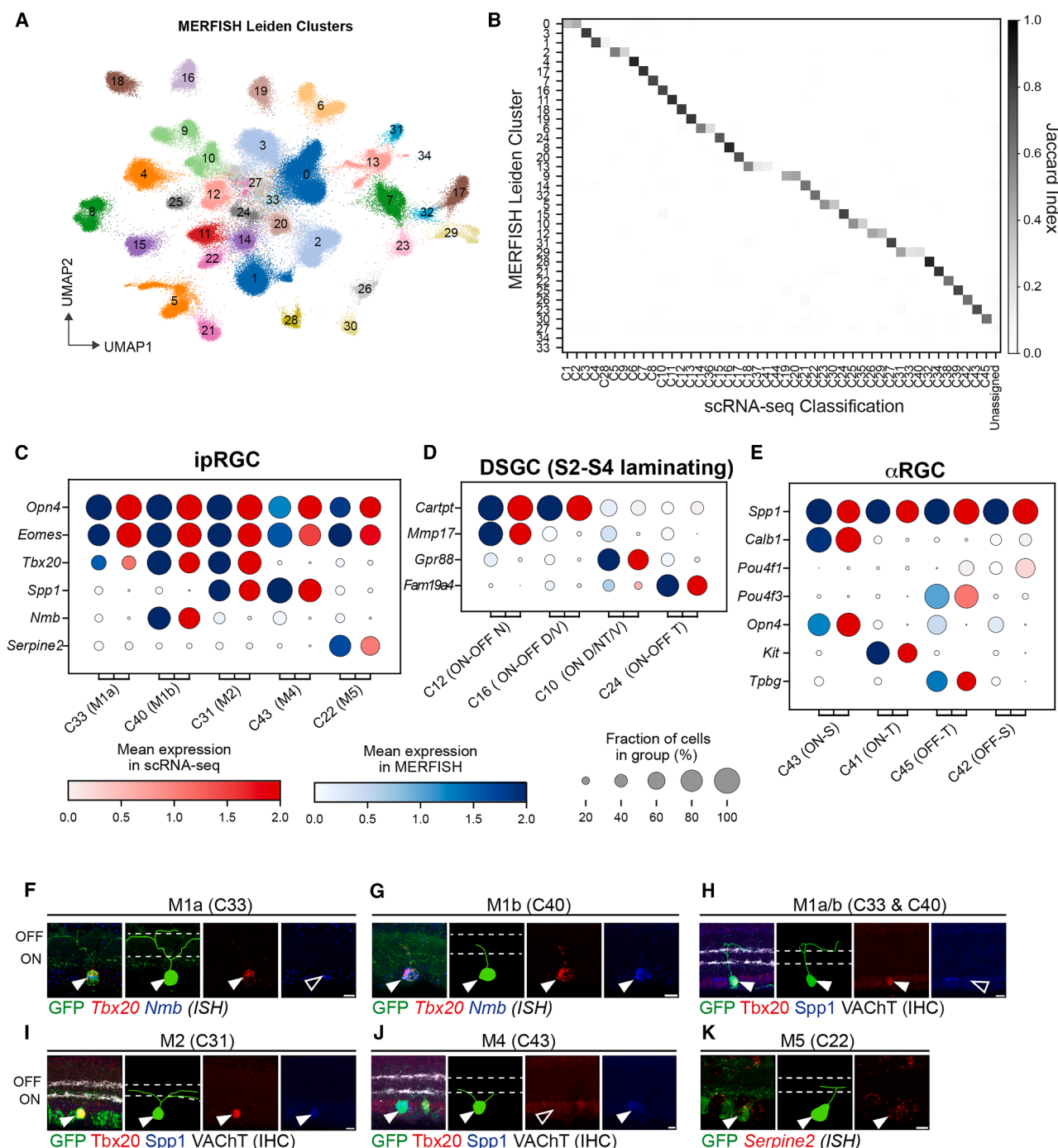


**Figure 3. MERFISH-based RGC-type classification and histological validation of ipRGC types**

(A) UMAP visualization of 35 MERFISH-based RGC clusters.

(B) Confusion matrix showing transcriptomic correspondence between MERFISH clusters 1–35 (rows) and RGC types C1–C45 (columns). Darker gray shading indicates higher correspondence, quantified by the Jaccard index.

(C–E) Dot plots comparing the transcriptomic fingerprints for three RGC subclasses between MERFISH (blue) and scRNA-seq (red). The size of each dot corresponds to the fraction of cells in each group that express the gene, and the color represents the average expression level.

(F and G) Fluorescent ISH using the Opn4-Cre; LSL-YFP line for ipRGC clusters,<sup>51</sup> C33 and C40, corresponding to M1a and M1b. *Tbx20<sup>+</sup>Nmb<sup>−</sup>* YFP<sup>+</sup> C33 (M1a) RGCs (F) and *Tbx20<sup>+</sup>Nmb<sup>+</sup>* YFP<sup>+</sup> C40 (M1b) RGCs (G) exhibit OFF dendrites characteristic of M1 ipRGCs.

(legend continued on next page)

separation of major cell classes in the GCL, we now focus on dissecting the molecular diversity within RGCs using the MERFISH data.

### Consistent profiles and frequencies of RGC types between MERFISH and scRNA-seq data

*De novo* clustering based on the measured gene panel identified 35 RGC clusters (**Figure 3A; STAR Methods**). We applied a supervised classification approach to assign adult RGC-type identities to these clusters, training the classifier on our previous scRNA-seq atlas,<sup>12</sup> using only the genes present in the current MERFISH panel as features. The scRNA-seq atlas comprises 45 RGC clusters (C1–C45), approximately half of which have been previously shown to map 1:1 to RGC types defined by morphology and physiology.<sup>10–12</sup> Small sets of RGC types sharing functional, molecular, and morphological features have been termed subclasses. Well-characterized subclasses include the DSGCs, comprising three On types and four On-Off types<sup>48</sup>; six types of ipRGCs, whose expression of melanopsin (*Opn4*) enables them to detect visual inputs directly, independent of rods and cones<sup>51,52</sup>; four types of αRGCs, identified by their characteristically large somata,<sup>53,54</sup> with On-sustained αRGCs being M4 ipRGCs (see below); and five types of *Foxp2*<sup>+</sup> F-RGCs.<sup>36</sup> **Table S2** summarizes these subclasses, stratifying the types within each subclass based on the current knowledge of their combined transcriptomic, morphological, and functional identities.

Overall, the correspondences between MERFISH clusters and transcriptomic types were highly specific (**Figures 3B** and **S2A**): of the 35 MERFISH clusters, 24 mapped 1:1 to a single RGC type, 8 clusters mapped to 2–3 types, and 3 could not be classified due to low transcriptomic quality but possessed RGC markers. As three examples of multi-mapping: (1) MERFISH cluster 29 contained scRNA-seq types C31, C33, and C40, which correspond to *Opn4*<sup>+</sup> ipRGC types M1 and M2 (see below), (2) MERFISH cluster 1 mapped to C4 and C28, corresponding to the F-RGC types, F-mini-Off and F-midi-Off, respectively,<sup>36</sup> and (3) MERFISH cluster 8 contained the D- and V-responsive On-Off DSGCs,<sup>37</sup> which are both present in the scRNA-seq type C16 but can be distinguished by the markers *Calb1* and *Calb2* (**Figures 3A, S2A**, and **S2B**). A closer examination suggested that all cases of multi-mapping involved the co-clustering of closely related types, which could be further resolved using supervised analyses. Specifically, the classifier enabled us to transfer scRNA-seq cluster labels (C1–C45) onto the MERFISH dataset. As a post hoc assessment of the label transfer, we examined the gene expression patterns and relative frequencies of matched RGC types between MERFISH and scRNA-seq. **Figures 3C–3E** and **S2C** show concordant gene expression fingerprints for four RGC subclasses: ipRGCs, On-Off DSGCs, αRGCs, and F-RGCs, respectively. Notably, these comparisons also revealed that a small subset (10/140) of the

MERFISH probes were not effective in detecting transcripts (**Figure S2D**). Nonetheless, the label transfer procedure was robust to these probe failures due to its reliance on multi-gene patterns, as excluding these probes only slightly improved the results.

Relative frequencies of the 45 RGC types were consistent among MERFISH replicates and correlated well with scRNA-seq frequencies,<sup>12</sup> except for low-frequency types with large somata, particularly the αRGC types (**Figure S2E; Table S2**). To clarify this discrepancy, we counted αRGCs in total, alongside the individual On-sustained αRGC type (C43) in separate retinas. These measurements validated that the MERFISH-based frequencies are more accurate for RGCs with large somata (**Figures S2F** and **S2G**). In contrast, scRNA-seq likely underestimates these RGCs with large somata, at least partially due to the fact that large cells are inefficiently recovered during microfluidics-based cell capture.<sup>55,56</sup>

Finally, we also estimated soma volumes for RGC types from MERFISH images and compared them with prior estimates from EM for cross-annotated types<sup>32</sup> (**Figures S2H** and **S2I**). While the rank order of the soma volumes correlated well between the two datasets, MERFISH-based soma volume estimates for large RGC types, such as αRGCs, were systematically lower than EM estimates due to segmentation challenges (**Figure S2H**), even though αRGCs had the highest soma volumes (**STAR Methods**). By contrast, soma volume estimates in MERFISH were accurate for smaller RGC types, such as F-RGCs<sup>36</sup> (**Figure S2H**). Overall, these results show that the quality of RGC classification in MERFISH aligns favorably with existing transcriptomics and morphology-based classification data.

### Annotation of ipRGC types

We leveraged these results to match molecular signatures to morphology for ipRGC clusters, all of which were defined by the expression of *Opn4*, the gene encoding melanopsin (**Figure 3C**). Previous work has identified six ipRGC types in mice, named M1–M6.<sup>52,57,58</sup> Our prior scRNA-seq atlas suggested putative annotations of *Opn4*<sup>+</sup> clusters to ipRGC types: C33 and C40, which express the highest levels of *Opn4*, were labeled M1a and M1b; C31 as M2; C43 as M4, also known as the On-sustained αRGC; C22 as either M3,<sup>59</sup> M5, or M6. Two other clusters, C7 and C8, express low levels of *Opn4* but are positive for the transcription factor *Eomes* (*Tbr2*), a molecular marker relatively restricted in the ipRGC subclass during development.<sup>22,60</sup>

Although ipRGCs are defined transcriptomically based on *Opn4* expression, antibodies against melanopsin have traditionally been noted to mark M1–M3, but not M4–M6, types without amplification.<sup>61</sup> Notably, M3 ipRGCs are relatively scarce in abundance<sup>59,62,63</sup> and are likely not represented in our dataset. We incorporated anti-*Opn4* immunostaining in our MERFISH experiments on the GCL and computed the intensity of antibody

(H) Immunohistochemistry (IHC) experiments show that *Tbx20*<sup>+</sup>*Spp1*<sup>−</sup>*YFP*<sup>+</sup> RGCs (M1a/b) are Off-laminating.

(I and J) IHC shows that *Tbx20*<sup>+</sup> *Spp1*<sup>+</sup> *YFP*<sup>+</sup> C31 (M2) RGCs are On-laminating with small soma size (I), while *Tbx20*<sup>−</sup> *Spp1*<sup>+</sup> *YFP*<sup>+</sup> C43 (M4) are On-laminating with large soma size (J).

(K) ISH showing that *Serpine2*<sup>+</sup> *YFP*<sup>+</sup> C22 (M5) RGCs are ON-laminating. Scale bars (F–K), 5 μm.

See also **Figures S2** and **S3** and **Table S2**.

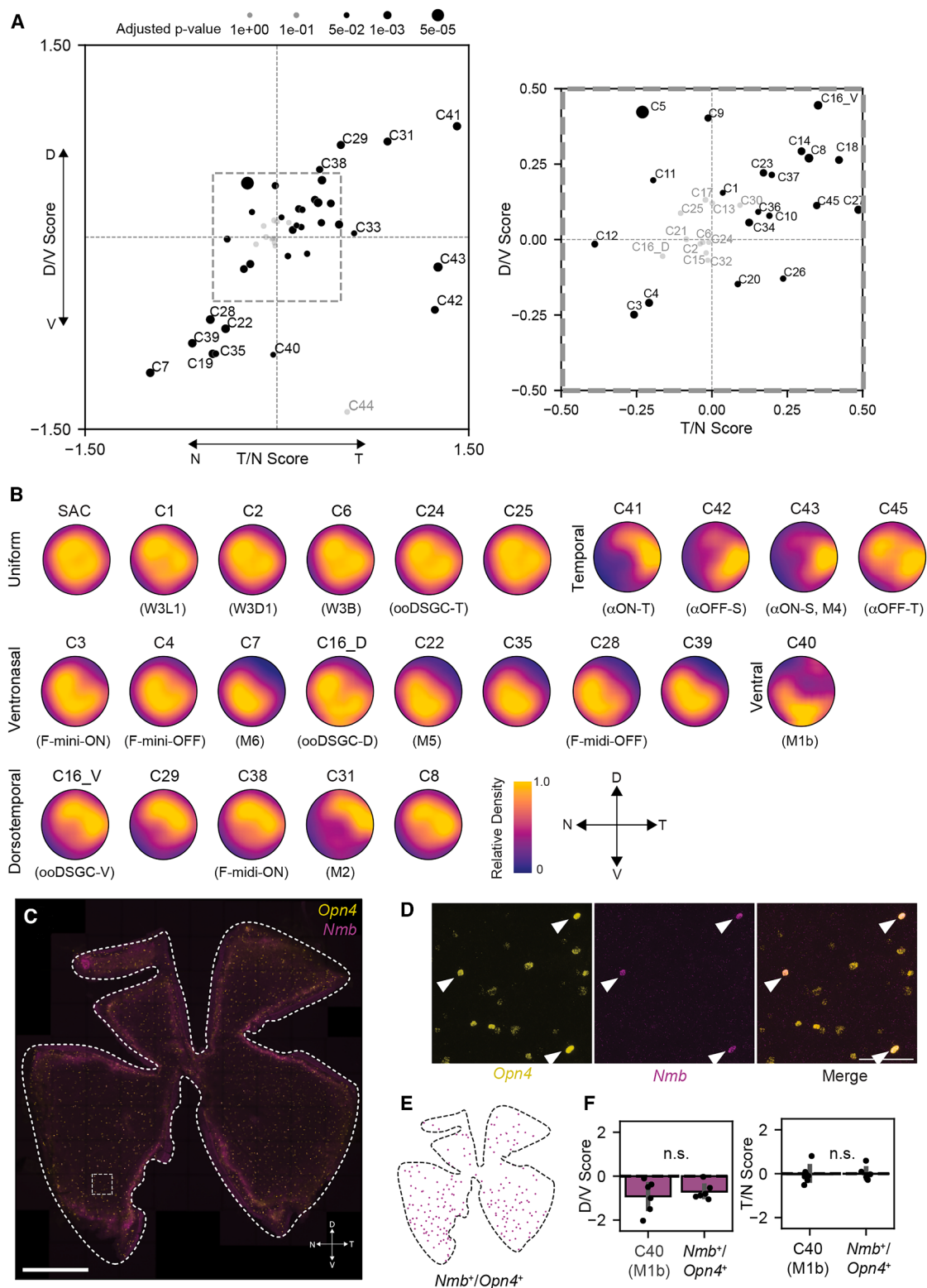


**Figure 4. Topographic distributions of RGC types**

(A) Scatterplot of the D/V (top to bottom, y axis) and T/N (x axis, left to right) scores for RGC types. Statistically significant deviations (Welch's t test, Benjamini-Hochberg correction) are highlighted in black, with larger dots for lower  $p$  values. The inset (right) zooms in on types near the origin.

(legend continued on next page)

staining within each molecularly defined RGC cluster (Figure S3A; **STAR Methods**). We found that clusters C31, C33, and C40, which expressed the highest level of *Opn4* transcripts, also exhibited the highest intensity for anti-*Opn4* immunohistochemistry (Figures S3A–S3D), consistent with these clusters comprising M1 and M2 ipRGCs. By performing fluorescent *in situ* hybridization (ISH) in a genetic line that marks all major ipRGCs (*Opn4-Cre*; Lox-Stop-Lox-Yellow Fluorescent Protein [LSL-YFP]), we verified that both C33 (YFP<sup>+</sup>*Tbx20*<sup>+</sup>*Nmb*<sup>-</sup>) and C40 (YFP<sup>+</sup>*Tbx20*<sup>+</sup>*Nmb*<sup>+</sup>) possess dendrites that laminated in the S1 sublamina of the inner plexiform layer (IPL) (Figures 3F and 3G), which are the hallmark of M1 ipRGCs. Moreover, YFP<sup>+</sup>*Spp1*<sup>-</sup>*Tbx20*<sup>+</sup>, encompassing both C33 and C40, were Off-laminating, validating their posited identity as M1 ipRGCs (Figure 3H). Among other ipRGC clusters, C31 and C43 express *Spp1* (Figure 3C). We found that YFP<sup>+</sup>*Tbx20*<sup>+</sup>*Spp1*<sup>+</sup> RGCs (C31) and YFP<sup>+</sup>*Tbx20*<sup>+</sup>*Spp1*<sup>+</sup> RGCs (C43) possessed S4/5 laminating dendrites, indicative of On-RGCs (Figures 3I and 3J). The soma sizes of C43 RGCs were larger, consistent with these being M4 ipRGCs (ON-sustained αRGCs). Therefore, YFP<sup>+</sup>*Tbx20*<sup>+</sup>*Spp1*<sup>+</sup> cells (C31), with smaller soma sizes, correspond to M2. *Spp1* was first characterized as a marker covering all αRGCs. As an addition, we verified that *Tbx20*<sup>+</sup>*Spp1*<sup>+</sup> RGCs did not co-label YFP<sup>+</sup> RGCs in the αRGCs marking line (*Kcng4-Cre*: LSL-YFP)<sup>25,53</sup> (Figures S3E and S3F). Finally, we found that YFP<sup>+</sup>*Serpine2*<sup>+</sup> RGCs possess S5 ON-laminating dendrites, identifying C22 as M5 ipRGCs (Figure 3K). Taken together, these results identify four ipRGC types among our transcriptomic clusters: M1 (C33, C40), M2 (C31), M4 (C43), and M5 (C22). C33 and C40 represent two M1 subtypes, with C40 (M1b) exhibiting higher levels of melanopsin immunoreactivity than C33 (M1a). A recent study has linked C7 with M6.<sup>63</sup> This still leaves the molecular identity of M3 open. M3 is a rare ipRGC type with bistratified dendrites,<sup>59</sup> whose transcriptomic identity remains unresolved.

### Topographic distributions of RGC types

Using the (x, y) coordinates in the MERFISH datasets, we examined the spatial distributions of each of the 45 RGC types on the retinal surface. For each RGC type, we assessed the topographic biases of somas along the D/V (represented vertically) and temporal-nasal axis (T/N, represented horizontally) axes (Figures 4A and 4B). By randomizing soma locations for each type in the dataset, we confirmed via simulations that unbiased distributions at all observed frequencies exhibit a mean score of zero along these axes (Figures S4A and S4B). We then quantified D/V and T/N biases for each RGC type, finding these scores to be highly consistent across the six replicates (Figures S4A and S4B).

(B) SAC and representative RGC-type distributions grouped by uniform, temporal, ventral, or dorsal biases, with adjusted density plots accounting for sampling inhomogeneity.

(C and D) Whole-mount ISH for *Opn4* (yellow) and *Nmb* (purple) marking C40 cells, with D/V and T/N orientations (C). The magnified view (D) shows *Nmb*<sup>+</sup> cells as a subset of *Opn4*<sup>+</sup> cells. Scale bars: 1 mm in (C) and 100 μm in (D).

(E) Ventrally biased spatial distribution of *Nmb*<sup>+</sup>*Opn4*<sup>+</sup> cells in (C).

(F) Comparison of D/V scores (left) and T/N scores (right) for C40 (*Nmb*<sup>+</sup>*Opn4*<sup>+</sup>) between MERFISH and FISH. Statistical significance was assessed using the Welch's t test ( $p > 0.05$ ), n.s., not significant.  $n = 6$  retinas each. Error bar: mean  $\pm$  1 SD.

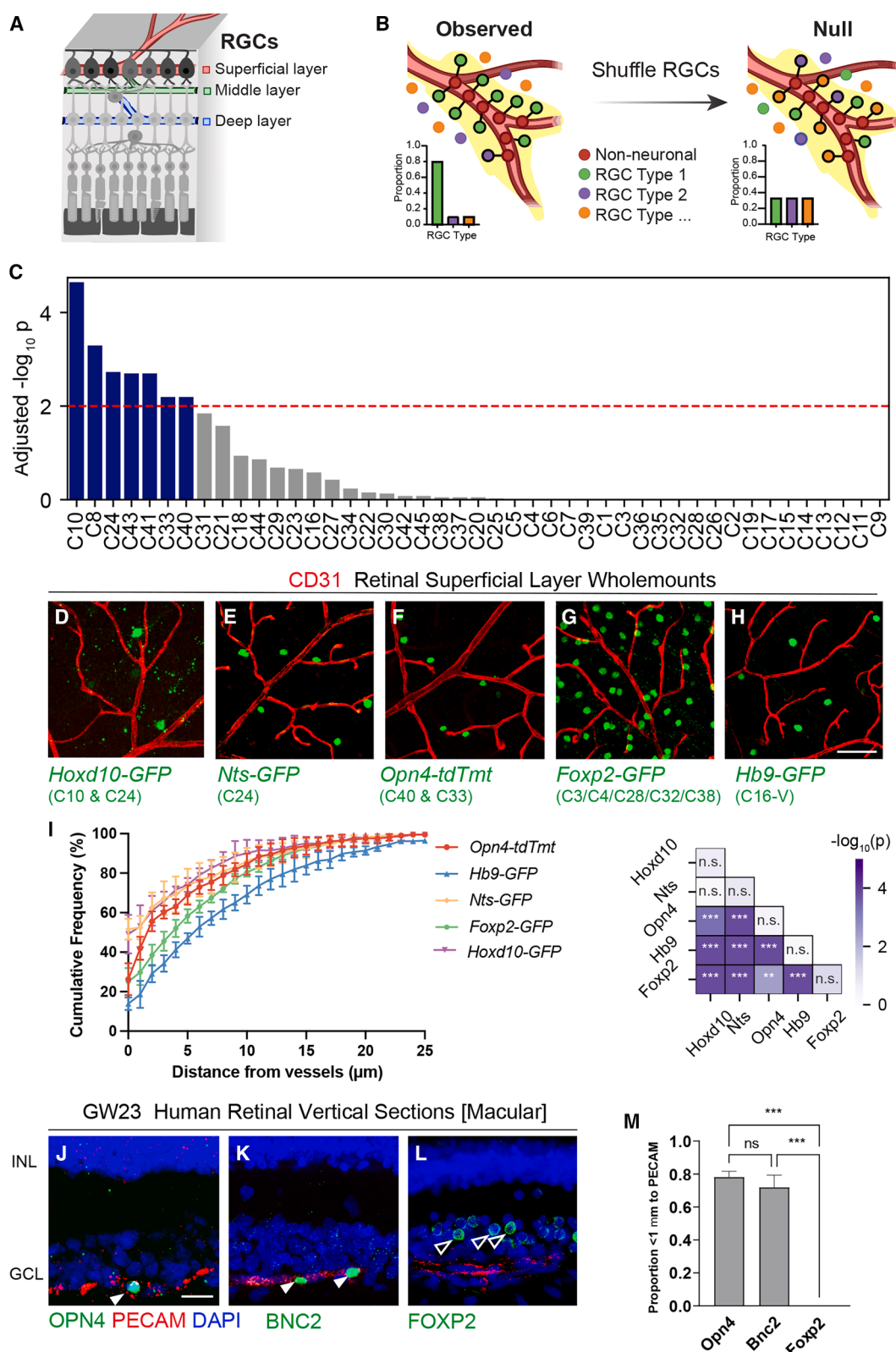
See also Figures S4 and S5.

Collectively, 34 out of the 45 RGC types (~75%) showed statistically significant topographic biases along the D/V or T/N axes or both. Notably, 14 types exhibited particularly strong biases (as defined by having a D/V or T/N score exceeding  $\pm 0.5$ ), underscoring pervasive topographic variations among RGC types (Figures 4A and 4B). Intriguingly, the biases were predominantly concentrated along the dorsal-temporal and ventral-nasal axes, with a few types skewed toward the temporal quadrant (Figures 4A and 4B). The average topographies for types are represented in Figures 4B and S4C. Our findings align with previously reported topographic analyses<sup>35</sup> and report additional ones. For example, three F-RGC types, C3, C4, and C28, corresponding to F-mini-On, F-mini-Off, and F-midi-Off types, exhibit ventral-nasal biases (Figures 4B and S4C). In contrast, C38 (F-midi-On) exhibits a dorsal-temporal bias.<sup>36</sup> Additionally, αRGC types (C41, C42, C43, and C45) displayed a temporal bias (Figures 4C and S4C), though C45 (Off-transient αRGCs) showed less bias than previously described (Figure S4C).<sup>34</sup>

Among ipRGC types, several exhibited notable biases, which align with frequency estimates from previous studies<sup>64</sup>: M2 (C31) was dorsal-temporal biased, M4 (On-α sustained) was temporal, and M5 was ventral-nasally biased (Figures 4A, 4B, and S4D). M1a exhibited a slight temporal skew, while M1b (C40) was biased ventrally. The ventral skew of M1b (C40) is consistent with a recent report showing that ventral M1 cells exhibit a higher intensity of melanopsin immunoreactivity.<sup>64</sup> C7, which putatively aligns with M6,<sup>63</sup> is strikingly ventral-nasal biased (Figure 4B). To further validate our findings, we performed double fluorescent ISH on retinal flatmounts, focusing on C40 (*Nmb*<sup>+</sup>*Opn4*<sup>+</sup>) (Figures 4C and 4D). We confirmed that *Nmb* co-labels with *Opn4*<sup>+</sup> RGCs were more frequently in the ventral than in the dorsal retina, and the estimated D/V and T/N scores corroborated our MERFISH-based estimates (Figures 4E and 4F). Finally, the topographic distributions of M1, M2, and M4–M6 ipRGC types in our data were consistent with those identified in a recently published transgenic line<sup>63</sup> (Figure S4D). Overall, these findings reveal that topographic bias is a prevalent and defining feature among RGC types, with distinct spatial preferences along the dorsal-temporal and ventral-nasal axes.

### Regularity in the somal spacing of RGC types

A widely accepted principle of retinal organization is that bona fide cell types form “mosaics” on the retinal surface,<sup>30</sup> with somas of the same neuronal type less likely to be adjacent than expected by random chance but randomly distributed relative to somas of other neuronal types.<sup>65</sup> Mosaic arrangements are thought to ensure equitable representation of visual features



(legend on next page)

across the retina, minimizing redundancy.<sup>9,66</sup> Although mosaicism has been extensively studied for some outer and inner retinal neuron types, such as SACs in the inner nuclear layer, cone PRs, and HCs,<sup>31,67–70</sup> comprehensive analyses of mosaic arrangements across all RGC types using consistent criteria remain largely unexplored, with prior studies focusing only on a limited number of RGC subsets identified through genetic or histological markers.<sup>5</sup>

Using our spatial maps, we calculated nearest-neighbor regularity indices (NNRIs) for 33 high-frequency RGC types and compared these against “null” NNI distributions observed in matched randomized simulations. While past studies generated a null distribution through the random placement of cells within regions of interest,<sup>31,68,71,72</sup> we observed that null NNI distributions are influenced by several technical factors. These include not only variations in soma size and density as observed previously<sup>31</sup> but also the presence of internal exclusion areas (IEAs) such as blood vessels, NN somas, and holes arising from sectioning. IEAs in particular tended to result in lower null NNI values. To ensure that our randomized simulations respect IEAs, we devised an approach where the RGC-type labels are permuted among RGC somas, whose locations are held fixed (Figures S5A–S5C; STAR Methods). This label-permutation approach results in lower null NNRIs (~1.9) than the previous method,<sup>31</sup> likely due to the constraint in soma positions and IEAs mentioned above. Roughly 75% of tested RGC types showed higher NNRIs than their matched nulls (Figures S5D–S5G), indicating some degree of spatial regularity. The extent of regularity, however, varied by type, and based on the gap between the observed NNI and the highest NNI in null simulations, appears to be modest relative to the highly ordered mosaics of PRs or HCs.<sup>4,31</sup> Consistent with previous work, types C3, C4, and the On-sustained  $\alpha$ RGC (C43) (Figures S5B, S5D, and S5E),<sup>34,36</sup> but also less well-characterized types such as C2, C11, and C32, displayed reliably regular spacing (Figures S5D' and S5E'). By contrast, C10—an aggregate of three transcriptomically indistinguishable On-DSGC subtypes—showed consistently low regularity<sup>10,48</sup> (Figures S5D and S5C). Simulations that involved mixing different “true” cell types *in silico* reduced NNI values, mirroring the low regularity of C10 (Figure S5F). Overall, the observed distributions were only

slightly more regular than their matched randomizations; yet, the differences were consistent and statistically significant. Additionally, different RGC types showed considerable variation in their regularity (Figure S5G). Because this effect is far milder than the highly ordered mosaics of PRs, inner nuclear layer SACs, and HCs, we describe it as weak regularity rather than mosaicism.

### Uncovering perivascular RGC types

Mammalian central neurons, including retinal neurons, are typically within 20  $\mu$ m of blood vessels to ensure oxygen and nutrient supply for high metabolic demands.<sup>73</sup> The retina contains a three-dimensional vascular lattice comprising three planar layers—superficial, middle, and deep—interconnected by penetrating vessels<sup>74</sup> (Figure 5A). In our data, more than 90% of NNs were identified as vasculature-associated cell types, including endothelial cells, pericytes, and astrocytes (Figure 2H), which enabled us to trace blood vessels within the SL (Figure 2I). This provided a foundation for analyzing the vascular proximity statistics of each RGC type on the 2D space harboring both vascular SL and GCL. Using a nearest-neighbor permutation test (STAR Methods), we identified 7 out of 45 RGC types that were significantly enriched for proximity to blood vessels (Figures 5B and 5C). 5 of these types belong to two major RGC subclasses: (1) ipRGCs—C33 (M1a), C40 (M1b), C43 (M4)—and (2) DSGCs—C10 (On-DSGCs) and C24 (temporal-On-Off DSGCs). Notably, we had previously identified C24 as perivascular RGCs using a candidate-based approach and revealed the specific role of C24 in forming the three-dimensional vascular lattice in developing retinas.<sup>75</sup> The MERFISH-based survey not only confirms the perivascularity of C24 but also systematically identifies the enrichment of additional RGC types within the perivascular niche.

To validate the computational results from MERFISH, we resorted to transgenic GFP (or RFP) labeling to characterize these perivascular RGC subsets.<sup>16,17,25,26</sup> Nts-GFP, which specifically marks *Fam19a4/Nts*<sup>+</sup> C24 RGCs, served as a positive control.<sup>75</sup> We found that 52.5%  $\pm$  5.9% of Nts-GFP<sup>+</sup> somata were located within 1  $\mu$ m of CD31<sup>+</sup> blood vessels (Figures 5E and 5I). Following this threshold, we subsequently categorized RGCs as perivascular if they were located within 1  $\mu$ m of CD31<sup>+</sup> blood

**Figure 5. Identification and characterization of perivascular RGC types**

- (A) Schematic showing three retinal vascular plexuses.
- (B) Permutation test schematic: random shuffling of RGC-type labels generates a null distribution (right) to test the proximity of each RGC type to CD31<sup>+</sup> retinal endothelial cells.
- (C) Permutation test results highlighting that perivascular RGC types ( $p < 0.01$ ) are enriched in two major RGC subclasses: ipRGCs (C40, C33, and C43) and DSGCs (C24, temporal-ooDSGCs; C10, On-DSGCs).
- (D–H) Validating predicted perivascular enrichment of RGC types: *Hoxd10*-GFP (C10, C24 in D), *Nts*-GFP (C24 in E), and *Opn4*-tdTomato (C40, C33 in F). *Foxp2*-GFP RGCs (C3/C4/C28/C32/C38 in G) and *Hb9*-GFP RGCs (C16-V in H) are not enriched in the perivascular space. Scale bars: 50  $\mu$ m.
- (I) (Left) Cumulative frequency distributions (CFDs) of nearest soma-vascular distances across the five lines listed in (D)–(H). (Right) Heatmap summarizing  $p$  values of statistical comparisons of the CFDs on the left panel. On the diagonal: k-sample Anderson-Darling test for the hypothesis that CFDs corresponding to each biological replicate from a given line correspond to a single underlying distribution. The null hypothesis is not rejected for any line ( $p > 0.05$  [n.s.]), highlighting the consistency across replicates. Off-diagonal terms: pairwise comparisons of CFDs between lines using the Anderson-Darling test with the Benjamini-Hochberg multiple testing correction, \*\*\* $p < 0.001$ , \*\* $p < 0.01$ . The null hypothesis is rejected for all comparisons except *Hoxd10*-GFP vs. *Nts*-GFP.  $n = 4$  animals each, error bars are SDs.
- (J–M) ISH in the macular region of the human prenatal retina (GW 22–23) showing perivascular enrichment of *OPN4*<sup>+</sup> ipRGCs (J, hRGC12) and *BNC2*<sup>+</sup> On-DSGCs (K, hRGC11), compared with non-enriched *FOXP2*<sup>+</sup> F-RGCs (L, hRGC6, hRGC7). The proportion of RGCs within 1  $\mu$ m of PECAM<sup>+</sup> (CD31<sup>+</sup>) vessels is shown for each group in (M). Scale bars: 20  $\mu$ m.  $n = 3$  human samples each, one-way ANOVA test, \*\*\* $p < 0.001$ . Data are presented as mean  $\pm$  SD.
- See also Figure S6.

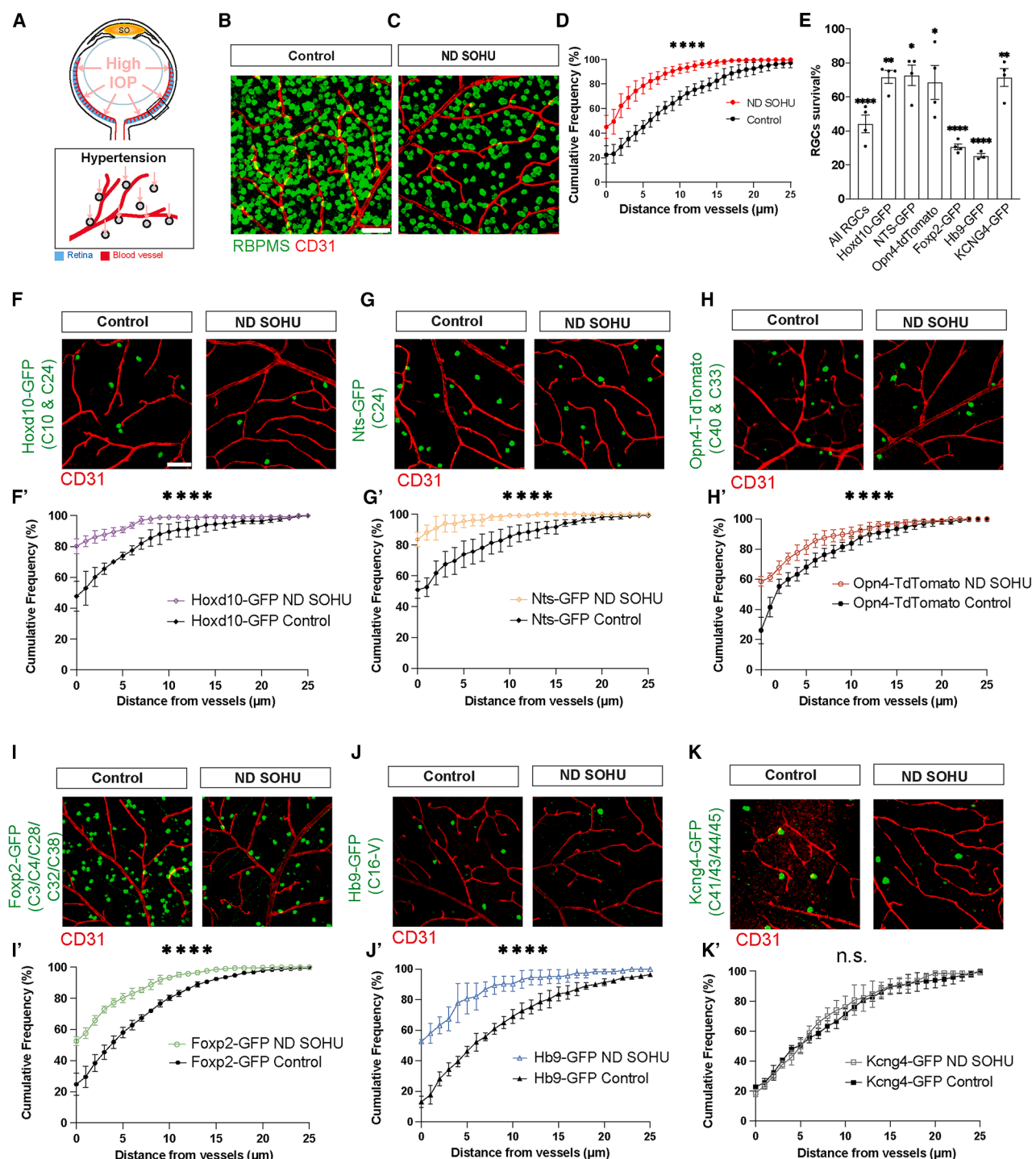


**Figure 6. Perivasculär RGC types exhibit preferential survival and enrichment in the perivasculär niche under experimental glaucomatous conditions**

(A) Schematic illustration of no-pupillary-dilation (ND) SOHU experiments (SO, silicone oil) to achieve elevated IOP.

(B-D) Sample images showing enrichment of RGCs in the perivasculär niche subject to ND SOHU treatment (C) at 3 wpi, compared with controls (B), as quantified in (D) using the CDFs along the perivasculär distance. Anderson-Darling test,  $n = 6$  animals each, \*\*\* $p < 0.0001$ .

(E) Quantifications showing that percentages of RGCs surviving at 3 wpi are higher in Hoxd10-GFP (C10 and C24), Nts-GFP (C24), Opn4-TdTomato (C40 and C33), and Kcnq4-GFP (C41, C42, C43, and C45) compared with Foxp2-RGCs (C3, C4, C28, C32, and C38), or Hb9-GFP RGCs (C16), or general RGCs

(legend continued on next page)

vessels. Next, we examined an established bacterial artificial chromosome (BAC) transgenic mouse line, Hoxd10-GFP,<sup>76</sup> which labels subsets of On-DSGCs (C10, *Gpr88<sup>+</sup>*) as well as some temporal On-Off DSGCs (i.e., *Fam19a4<sup>+</sup>* C24 RGCs) (Figure 3D).<sup>75,76</sup> ISH confirmed that Hoxd10-GFP<sup>+</sup> RGCs consist of 54.4% ± 2.7% *Gpr88<sup>+</sup>* cells (C10) and 32.5% ± 5.6% *Fam19a4<sup>+</sup>* cells (C24) (Figures S6A, S6B, and S6D). In contrast, these cells stained negative for conventional On-Off DSGC histology markers, including *Cartpt* (Figures S6C and S6D).<sup>77</sup> 53.2% ± 10.6% of Hoxd10-GFP<sup>+</sup> RGC somata, which are a mixture of C10 and C24 cells, were within 1 μm of CD31<sup>+</sup> blood vessels (Figures 5D and 5I). Notably, at single RGC-type resolution, C24 (Figures 5E and 5I), and C10 (Hoxd10-GFP<sup>+</sup> Nts-RFP<sup>-</sup>) (Figures S6G and S6H) were as perivascular as Hoxd10-GFP<sup>+</sup> RGCs. In parallel with DSGCs, we also investigated the perivascular location of ipRGCs, as identified in Figure 5C. Instead of the *Opn4-Cre* line that marks all ipRGCs, we examined the *Opn4-tdTomato* BAC transgenic line, which dominantly and brightly labels M1 (C33, C40) (Figures S6E and S6F),<sup>78</sup> in order to specifically target the perivascular ipRGC types. 41.9% ± 5.8% of *Opn4-tdTomato*<sup>+</sup> RGC somata were within 1 μm of CD31<sup>+</sup> vessels (Figures 5F and 5I). As controls, we analyzed Hb9-GFP<sup>+</sup> RGCs, which comprise ventral On-Off DSGCs (C16-V). Only 13.8% ± 3.2% of Hb9-GFP<sup>+</sup> RGC somata were within 1 μm of blood vessels, indicating a substantially lower degree of perivascularity (Figures 5H and 5I). Among *Foxp2-GFP*<sup>+</sup> RGCs (C3, C4, C28, C32, and C38), ~25.2% ± 6.9% somata were within 1 μm of CD31<sup>+</sup> vessels (Figures 5G and 5I). In summary, our results validate the MERFISH findings regarding several newly defined perivascular RGC types. We also characterized two transgenic lines that can be utilized to investigate perivascular RGCs *in vivo*: Hoxd10-GFP partially labels C10 On-DSGCs and C24 temporal On-Off DSGCs, while *Opn4-tdTomato* labels C33 and C40 M1a/b ipRGCs but also includes C31 M2 ipRGCs.

### Evolutionarily conserved perivascular RGC types in the human retina

ipRGCs and On-DSGCs are RGC types with conserved molecular profiles across mice and humans.<sup>79–81</sup> We next examined whether these spatially restricted perivascular RGC types in mice—such as ipRGCs and On-DSGCs—are similarly perivascular in the human retina. OPN4 (melanopsin) marks the transcriptomic ortholog, hRGC12, of mouse ipRGCs (M1 and M2),<sup>24,79</sup> while BNC2 marks hRGC11, a human On-DSGC cluster orthologous to the mouse C10 DSGC cluster.<sup>79,81</sup> To explore the perivascularity of human RGC clusters, we selected OPN4 and BNC2 as candidate markers. We focused on prenatal retinas,

macular regions in particular, during gestational weeks (GWs) 22–23, a period of active retinal angiogenesis and neuronal growth.<sup>82</sup> The human prenatal macular region contains multiple layers of RGCs, with blood vessels in the proximity of the bottom layer (Figures 5J–5L). It provides a convenient anatomical assay for examining the perivascularity at this stage. Using such prenatal retina tissues, we detected high mRNA expression of OPN4 and BNC2 in RGCs within the GCL. 78.2% ± 3.5% of OPN4<sup>+</sup> RGCs were located within 1 μm of PECAM(CD31)<sup>+</sup> vessels (Figures 5J and 5M), mirroring the perivascular localization of ipRGCs in mice (Figures 5F and 5I). Similarly, 72.0% ± 7.4% of BNC2<sup>+</sup> RGCs were found near CD31<sup>+</sup> vessels (Figures 5K and 5M), closely resembling the perivascular pattern observed in mouse C10 On-DSGCs (Figures 5D and 5I). As a control, human *Foxp2*<sup>+</sup> RGCs were non-perivascular and distributed away from the bottom layer of the RGCs (Figures 5L and 5M). Together, these results demonstrate that molecularly defined ipRGC and On-DSGC subsets are conserved perivascular RGC types in both mice and humans.

### Preferential RGC survival in the perivascular niche under an experimental glaucoma model

Using an unbiased scRNA-seq screen, we previously discovered that M1, M2, and M4 ipRGCs (C33, C40, C31, and C43), together with On-DSGCs (C10), are among the few RGC types selectively resilient following optic nerve crush (ONC).<sup>12</sup> Independent transgenic and histological studies have corroborated the selective survival of ipRGCs, On-DSGCs, and αRGCs after axotomy.<sup>25,29,83</sup> Although ONC is valuable for dissecting neuronal intrinsic injury responses, to our knowledge, it does not perturb retinal perfusion. It thus offers limited insights into whether vascular proximity may confer resilience. Moreover, while ONC is an extremely reliable model for traumatic injury, it may not model glaucoma closely, thereby limiting its direct relevance to pathophysiology. By contrast, the silicone oil-induced ocular hypertension under-detected (SOHU) model reproduces key features of secondary human glaucoma—sustained IOP elevation and widespread RGC loss<sup>26,84</sup>—while also exhibiting a measurable reduction in retinal blood flow in the no-pupillary dilation (ND) SOHU model, one of the two variants of SOHU glaucoma models with more acute and severe IOP elevation and neurodegeneration.<sup>85</sup> These properties made SOHU ideal for testing whether the perivascular niche confers neuroprotection when the vascular supply is compromised by ocular hypertension.

3 weeks post injections (3 wpi) in adult mouse eyes, overall vascular coverage in the GCL remained largely unchanged (Figures 6A and S6I–S6L). Yet, the surviving RGC population

(Rbpsm-positive). Each dot represents an individual retina. n = 4 retinas per group. Data are presented as means ± SEM. Statistical comparisons were performed between post-ND SOHU and controls using an unpaired two-sided Student's t test. \*p < 0.05, \*\*p < 0.01, \*\*\*p < 0.0001.

(F–J) Sample images between controls and ND SOHU 3 wpi. Survival of Hoxd10-GFP (F, C10 and C24), Nts-GFP (G, C24), and *Opn4-TdTomato* (H, C40 and C33) was higher compared with *Foxp2*-RGCs (I, C3, C4, C28, C32, and C38), and Hb9-GFP RGCs (J, C16), correlating with their perivascular distribution after ND SOHU treatment at 3 wpi. (F'–J') Perivascular enrichment was quantified similarly to (D), using the CFDs, with error bars indicating SD between biological replicates. For each line, CFDs were compared under controls and ND SOHU.

(K) *Kcnq4-GFP* αRGCs (C41, C42, C43, C45) exhibited resiliency under ND SOHU but did not exhibit perivascular enrichment after ND SOHU. n = 4 animals each.

(K') Comparison of CFDs, similar to (F').

Scale bars: 50 μm in (B), (C), and (F)–(K). Anderson-Darling test with the Benjamini-Hochberg multiple testing correction, n = 4 animals (F–K), \*\*\*\*p < 0.0001, n.s. p > 0.05.

See also Figure S6.

was markedly enriched in vessel-adjacent regions compared with controls (Figures 6B–6D). Notably, even ONC showed a perivascular enrichment of surviving RGCs. However, its extent was lower (Figures S6R–S6T), and the enrichment was absent in the lower tail of the distribution, unlike SOHU (compare Figures 6D and S6U). These observations suggest that certain RGC types may benefit specifically from the perivascular microenvironment under SOHU conditions. To test this hypothesis, we applied the ND SOHU model to the transgenic lines introduced in Figures 5D–5H. After ND SOHU, the three perivascular groups—Hoxd10-GFP (C10, C24), Nts-GFP (C24), and Opn4-tdTomato (C33, C40)—retained significantly more surviving RGCs compared with the general RGC population, while the non-perivascular controls—Hb9-GFP (C16-V) and Foxp2-RGCs (C3, C4, C28, C32, C38)—were depleted more substantially (Figure 6E). Cumulative frequency distributions (CFDs) in retinas co-stained with CD31 confirmed that all five groups shifted closer to vessels after injury. Still, the enrichment was greatest—and survival highest—for the types that were *a priori* enriched in the perivascular niche (Figures 6F–6J). Notably, although the proportion of cells right next to CD31<sup>+</sup> vessels was similar for Opn4-tdTomato RGCs and Foxp2-RGCs, the smaller median soma-to-vessel distance of the former (2 vs. 5 μm) partially explains their enhanced survival (Figures 6H and 6I).

We also analyzed the survival of αRGCs (C41, C42, C43, and C45) in ND SOHU using the Kcng4-GFP line.<sup>25</sup> Similar to what was reported in ONC<sup>25</sup> and high-frequency SOHU,<sup>26</sup> αRGCs also exhibit resilience in ND SOHU (Figure 6E); however, their spatial distribution relative to vessels remains unchanged (Figure 6K). Thus, the likely reason is that their protection hinges on high intrinsic mTOR/pS6 activity, as previously reported (Figures S6P and S6Q).<sup>25</sup> By contrast, mTOR/pS6 levels were low in Nts-GFP, Hoxd10-GFP, and Opn4-TdTomato RGCs (Figures S6M–S6O and S6Q), indicating that their survival does not rely on mTOR activity.<sup>29,86</sup> Taken together, these findings argue that the perivascular niche supplies an mTOR-independent extrinsic neuroprotective signal.<sup>12,25–29</sup>

## DISCUSSION

We combined MERFISH-based spatial transcriptomics with histological and computational methods to generate a comprehensive spatial atlas for mouse RGC types. By leveraging molecular signatures from scRNA-seq atlases, we mapped the *en face* distributions of 45 mouse RGC types, providing insights into their spatial arrangement and local microenvironments. Beyond validating the existing transcriptomic taxonomy of RGCs,<sup>12</sup> our study presents the spatial topographies of all 45 types at single-neuron resolution with minimal batch effects across adult mouse retinas.

On the technical side, our approach offers a high-throughput method for analyzing RGC taxonomy in intact wild-type retinas, thereby overcoming the limitations of previous transgenic or antibody-dependent methods. By capturing ~30,000 RGCs per retina, this method surpasses the throughput of scRNA-seq, which often requires pooling multiple retinas to compensate for the cell loss during enzymatic dissociation and microfluidic capture.<sup>12</sup> Compared with scRNA-seq, the MERFISH-based

method provides a more accurate estimate of neuronal type frequencies, particularly for neuronal types with large somata (Figures S2F and S2G; Table S2). Additionally, the *en face* preparation focuses specifically on the GCL, enabling precise analyses of RGC topographies, local spacing, and cell-cell interactions with the microenvironment. Our flatmount approach differs in several technical aspects from a recent spatial transcriptomic analysis of vertical retinal sections.<sup>87</sup> Additionally, our protocol preserves RNA quality for high-resolution spatial analyses. As demonstrated in this study, it enables the integration of antibody-based staining and transgenic markers in the MERFISH-based RNA environment, broadening its applicability.

Our results reveal that over 75% of RGC types exhibit non-uniform distributions across the retinal surface. While confirming previously noted patterns for specific subsets, such as Foxp2-RGCs and αRGCs, our results also suggest that this variability extends across most RGC types, thereby reinforcing the idea that topographic nonuniformity at the cell-type level may be a rule, rather than an exception, in the retina.<sup>9,35</sup> This non-uniformity likely influences the structure and function of associated retinal circuits, reflecting evolutionary adaptations to the mouse's visual environment. Combined with our growing understanding of the evolution of retinal cell types,<sup>24</sup> our current study provides a foundation for exploring the topographic arrangements of orthologous RGC types in species with distinct visual behaviors. In addition, by analyzing local neighborhoods, we provide evidence for regularity in inter-soma spacing among several RGC types. We note that for most types that appear regular compared with matched random simulations, the degree of regularity is modest compared with well-known mosaics in the retina.<sup>30,31</sup> Accordingly, we emphasize that our results should be interpreted as evidence for regularity, not proof of mosaicism.

Moreover, we also identified multiple RGC types enriched in perivascular niches, including members of the ipRGC and DSGC subclasses. These findings, validated using two transgenic lines (Hoxd10-GFP and Opn4-tdTomato), enabled further characterization of RGC types enriched in perivascular spaces. Perivascular ipRGCs and On-DSGCs exhibited enhanced survival following ND SOHU treatment, compared with non-perivascular RGCs, such as Foxp2-RGCs and Hb9-GFP RGCs. Furthermore, surviving RGCs preferentially distribute in the perivascular niche, compared with naive conditions. Thus, there is an enrichment of perivascular ipRGCs and On-DSGCs subject to ND SOHU treatment in the perivascular niche. At the same time, non-perivascular RGCs, such as Foxp2-RGCs and Hb9-RGCs, exhibit susceptibility to ND SOHU treatment due to a lower number of RGCs in the perivascular niche. Collectively, these data suggest that proximity to blood vessels may provide a neuroprotective advantage. This observation contrasts with the high-mTOR activity-dependent intrinsic neuroprotection seen in αRGCs,<sup>25,26</sup> pointing to distinct neuroprotective mechanisms mediated by the local vascular microenvironment. However, detailed mechanisms underlying neuroprotection remain to be identified. In the human retina, we find that orthologous counterparts of mouse M1 ipRGCs and On-DSGCs are also perivascular in the human retina, suggesting an evolutionarily conserved relationship between these RGC types and the perivascular niche. In addition,

whether or not ipRGCs (C40 and C33) and On-DSGCs (C10) influence vascular patterning in the developing retina, similar to C24 (Nts-RGCs),<sup>75</sup> remains to be explored. The underlying neurovascular interaction mechanisms remain to be examined.

We end by acknowledging some limitations of the current work that present opportunities for future developments. The analyses focused on a curated set of 140 marker genes, which limited the ability to capture genome-wide transcriptional patterns or classify non-RGCs, such as dACs and other NN types. Future advancements in spatial transcriptomics, with higher gene content and increased capture efficiency, will further expand the scope of such studies. Additionally, the use of thin tissue sections, while essential for the current approach, introduces experimental and data analysis challenges that ongoing advancements in thick-section imaging could alleviate.<sup>88,89</sup> These future endeavors would be especially helpful for more extensive testing of cell-cell spacing statistics than was feasible in this dataset. Nonetheless, our work establishes a robust framework for studying the spatial organization, taxonomy, and interactions of RGCs with the local microenvironment. By characterizing the spatial profiles of RGC types, we also linked neurodegenerative responses at individual neuron type resolution across the 2D space. This framework has implications for understanding retinal development, physiology, and neurodegeneration in mice and humans.

## RESOURCE AVAILABILITY

### Lead contact

Requests for further information, resources, and reagents should be directed to and will be fulfilled by the lead contact, Xin Duan ([xin.duan@ucsf.edu](mailto:xin.duan@ucsf.edu)).

### Materials availability

This study did not generate new, unique reagents.

### Data and code availability

- Post-segmentation MERFISH count matrices reported in this study are available via NCBI's Gene Expression Omnibus (GEO) accession number GEO: GSE303399.
- The final processed MERFISH dataset and statistics associated with this study were deposited at Zenodo: <https://doi.org/10.5281/zenodo.1634210>.
- All computational scripts detailing MERFISH analysis reported in this paper, as a version of the record, were deposited at Zenodo: <https://doi.org/10.5281/zenodo.1636997>; they are also available at <https://github.com/shekharlab/SpatialRGC>.
- All imaging data reported in the paper, including the raw data acquired at MERSCOPE, immunohistochemistry, and RNA scope images acquired at LSM Zeiss confocal, will be shared by the [lead contact](#) upon request.
- Any additional information required to reanalyze the data reported in this work paper is available from the [lead contact](#) upon request.

## ACKNOWLEDGMENTS

We thank J. He, X.K. Chen, L. Li, L. Zhang, D.S. Welsbie, T. Puthussery, M.B. Feller, and J.R. Sanes for advice; S. Varadarajan and K.W. Yau for sharing transgenics; and Y. Kuo, S. Wang, L. Pena, P. Miller, and H. Wang for support. We acknowledge P30EY002162 vision core, RPB fund to UCSF; F30EY033201 to N.Y.T.; BrightFocus Foundation Postdoctoral Fellowship (G2024005F) to M.Z.; K01MH123757 to A.T.E.; R35NS097305 to A.R.K.; F32EY033639 to F.C.-H.; R01EY023648, R01EY034089, R01EY036071,

and R01EY036430 to M.T.H.D.; R01EY032564 to B.S.; R01EY024932 and R01EY023295 to Y.H.; R01EY030138, R01EY019887 (PI, Gould), R01NS123912, U01NS136405, ARPA-H (VISION), and RPB Stein Award to X. D.; NSF CRCNS-2309039, Melza M. and Frank Theodore Barr Foundation, McKnight Foundation, and BrightFocus Foundation NGR to K.S.; and Catalyst for a Cure from Glaucoma Research Foundation to Y.H., X.D., and K.S.

## AUTHOR CONTRIBUTIONS

K.N., N.Y.T., M.Z., K.S., and X.D. conceived the study and wrote the manuscript, with all authors' input; N.Y.T. and X.D. optimized histology and RNA preparation; K.N. and K.S. established computational pipeline and analyzed the data; N.Y.T. and M.R.L. performed MERFISH reactions; M.Z., M.R.L., and Y.Y. performed immunohistochemistry; M.Z. and Y.H. performed animal surgeries; M.Z. and A.R.K. analyzed human donor tissues; T.R.G. and B.S. contributed to ipRGC histology; Y.W., K.T., A.T.E., N.R., F.C.-H., and M.T.H. D. contributed to genetic reagents and data analyses; and K.S. and X.D. co-supervised the study and acquired research funds.

## DECLARATION OF INTERESTS

The authors declare no competing interests.

## STAR★METHODS

Detailed methods are provided in the online version of this paper and include the following:

- KEY RESOURCES TABLE
- EXPERIMENTAL MODEL AND STUDY PARTICIPANT DETAILS
  - Genetically modified mouse lines for RGC subset labeling
  - Human retinal tissues
- METHOD DETAILS
  - Mouse retinal wholemount sectioning
  - MERFISH workflow using MERSCOPE
  - Mouse retina immunohistochemistry
  - Retinal RNAscope *in situ* hybridization
  - No-pupillary dilation silicone oil induced ocular hypertension under-detected model (ND SOHU)
  - Optic nerve crush (ONC) model
- QUANTIFICATION AND STATISTICAL ANALYSIS
  - Gene panel simulation
  - Preprocessing MERFISH data
  - GCL cell class verification via XGBoost
  - RGC classification
  - RGC spatial distributions in the 2D space
  - Perivascularity of RGC types
  - Local spatial analysis of each RGC type
  - Data acquisition and quantification for retinal immunohistochemistry data
  - Statistical methods

## SUPPLEMENTAL INFORMATION

Supplemental information can be found online at <https://doi.org/10.1016/j.neuron.2025.07.025>.

Received: December 11, 2024

Revised: May 31, 2025

Accepted: July 24, 2025

## REFERENCES

- Luo, L., Callaway, E.M., and Svoboda, K. (2018). Genetic Dissection of Neural Circuits: A Decade of Progress. *Neuron* 98, 865. <https://doi.org/10.1016/j.neuron.2018.05.004>.

2. Zeng, H., and Sanes, J.R. (2017). Neuronal cell-type classification: challenges, opportunities and the path forward. *Nat. Rev. Neurosci.* 18, 530–546. <https://doi.org/10.1038/nrn.2017.85>.
3. Kerschensteiner, D., and Feller, M.B. (2024). Mapping the Retina onto the Brain. *Cold Spring Harbor Perspect. Biol.* 16, a041512. <https://doi.org/10.1101/cshtperspect.a041512>.
4. Masland, R.H. (2001). The fundamental plan of the retina. *Nat. Neurosci.* 4, 877–886. <https://doi.org/10.1038/nn0901-877>.
5. Sanes, J.R., and Masland, R.H. (2015). The types of retinal ganglion cells: current status and implications for neuronal classification. *Annu. Rev. Neurosci.* 38, 221–246. <https://doi.org/10.1146/annurev-neuro-071714-034120>.
6. Shekhar, K., and Sanes, J.R. (2021). Generating and Using Transcriptomically Based Retinal Cell Atlases. *Annu. Rev. Vis. Sci.* 7, 43–72. <https://doi.org/10.1146/annurev-vision-032621-075200>.
7. Masland, R.H. (2012). The neuronal organization of the retina. *Neuron* 76, 266–280. <https://doi.org/10.1016/j.neuron.2012.10.002>.
8. Gollisch, T., and Meister, M. (2010). Eye smarter than scientists believed: neural computations in circuits of the retina. *Neuron* 65, 150–164. <https://doi.org/10.1016/j.neuron.2009.12.009>.
9. Baden, T., Berens, P., Franke, K., Román Rosón, M., Bethge, M., and Euler, T. (2016). The functional diversity of retinal ganglion cells in the mouse. *Nature* 529, 345–350. <https://doi.org/10.1038/nature16468>.
10. Goetz, J., Jessen, Z.F., Jacobi, A., Mani, A., Cooler, S., Greer, D., Kadri, S., Segal, J., Shekhar, K., Sanes, J.R., and Schwartz, G.W. (2022). Unified classification of mouse retinal ganglion cells using function, morphology, and gene expression. *Cell Rep.* 40, 111040. <https://doi.org/10.1016/j.celrep.2022.111040>.
11. Huang, W., Xu, Q., Su, J., Tang, L., Hao, Z.Z., Xu, C., Liu, R., Shen, Y., Sang, X., Xu, N., et al. (2022). Linking transcriptomes with morphological and functional phenotypes in mammalian retinal ganglion cells. *Cell Rep.* 40, 111322. <https://doi.org/10.1016/j.celrep.2022.111322>.
12. Tran, N.M., Shekhar, K., Whitney, I.E., Jacobi, A., Benhar, I., Hong, G., Yan, W., Adiconis, X., Arnold, M.E., Lee, J.M., et al. (2019). Single-Cell Profiles of Retinal Ganglion Cells Differing in Resilience to Injury Reveal Neuroprotective Genes. *Neuron* 104, 1039–1055.e12. <https://doi.org/10.1016/j.neuron.2019.11.006>.
13. Rheaume, B.A., Jereen, A., Bolisetty, M., Sajid, M.S., Yang, Y., Renna, K., Sun, L., Robson, P., and Trakhtenberg, E.F. (2018). Single cell transcriptome profiling of retinal ganglion cells identifies cellular subtypes. *Nat. Commun.* 9, 2759. <https://doi.org/10.1038/s41467-018-05134-3>.
14. Badea, T.C., Cahill, H., Ecker, J., Hattar, S., and Nathans, J. (2009). Distinct roles of transcription factors brn3a and brn3b in controlling the development, morphology, and function of retinal ganglion cells. *Neuron* 61, 852–864. <https://doi.org/10.1016/j.neuron.2009.01.020>.
15. Duan, X., Krishnaswamy, A., De la Huerta, I., and Sanes, J.R. (2014). Type II cadherins guide assembly of a direction-selective retinal circuit. *Cell* 158, 793–807. <https://doi.org/10.1016/j.cell.2014.06.047>.
16. Huberman, A.D., Manu, M., Koch, S.M., Susman, M.W., Lutz, A.B., Ullian, E.M., Baccus, S.A., and Barres, B.A. (2008). Architecture and activity-mediated refinement of axonal projections from a mosaic of genetically identified retinal ganglion cells. *Neuron* 59, 425–438. <https://doi.org/10.1016/j.neuron.2008.07.018>.
17. Kim, I.J., Zhang, Y., Meister, M., and Sanes, J.R. (2010). Laminar restriction of retinal ganglion cell dendrites and axons: subtype-specific developmental patterns revealed with transgenic markers. *J. Neurosci.* 30, 1452–1462. <https://doi.org/10.1523/JNEUROSCI.4779-09.2010>.
18. Siegert, S., Scherf, B.G., Del Punta, K., Didkovsky, N., Heintz, N., and Roska, B. (2009). Genetic address book for retinal cell types. *Nat. Neurosci.* 12, 1197–1204. <https://doi.org/10.1038/nn.2370>.
19. Krishnaswamy, A., Yamagata, M., Duan, X., Hong, Y.K., and Sanes, J.R. (2015). Sidekick 2 directs formation of a retinal circuit that detects differential motion. *Nature* 524, 466–470. <https://doi.org/10.1038/nature14682>.
20. Tsai, N.Y., Wang, F., Toma, K., Yin, C., Takatoh, J., Pai, E.L., Wu, K., Matcham, A.C., Yin, L., Dang, E.J., et al. (2022). Trans-Seq maps a selective mammalian retinotectal synapse instructed by Nephronectin. *Nat. Neurosci.* 25, 659–674. <https://doi.org/10.1038/s41593-022-01068-8>.
21. Martersteck, E.M., Hirokawa, K.E., Evarts, M., Bernard, A., Duan, X., Li, Y., Ng, L., Oh, S.W., Ouellette, B., Royall, J.J., et al. (2017). Diverse Central Projection Patterns of Retinal Ganglion Cells. *Cell Rep.* 18, 2058–2072. <https://doi.org/10.1016/j.celrep.2017.01.075>.
22. Shekhar, K., Whitney, I.E., Butrus, S., Peng, Y.R., and Sanes, J.R. (2022). Diversification of multipotential postmitotic mouse retinal ganglion cell precursors into discrete types. *eLife* 11, e73809. <https://doi.org/10.7554/eLife.73809>.
23. Whitney, I.E., Butrus, S., Dyer, M.A., Rieke, F., Sanes, J.R., and Shekhar, K. (2023). Vision-Dependent and -Independent Molecular Maturation of Mouse Retinal Ganglion Cells. *Neuroscience* 508, 153–173. <https://doi.org/10.1016/j.neuroscience.2022.07.013>.
24. Hahn, J., Monavarfeshani, A., Qiao, M., Kao, A., Kölsch, Y., Kumar, A., Kunze, V.P., Rasys, A.M., Richardson, R., Baier, H., et al. (2023). Evolution of neuronal cell classes and types in the vertebrate retina. Preprint at bioRxiv. <https://doi.org/10.1101/2023.04.07.536039>.
25. Duan, X., Qiao, M., Bei, F., Kim, I.J., He, Z., and Sanes, J.R. (2015). Subtype-specific regeneration of retinal ganglion cells following axotomy: effects of osteopontin and mTOR signaling. *Neuron* 85, 1244–1256. <https://doi.org/10.1016/j.neuron.2015.02.017>.
26. Zhao, M., Toma, K., Kinde, B., Li, L., Patel, A.K., Wu, K.Y., Lum, M.R., Tan, C., Hooper, J.E., Kriegstein, A.R., et al. (2023). Osteopontin drives retinal ganglion cell resiliency in glaucomatous optic neuropathy. *Cell Rep.* 42, 113038. <https://doi.org/10.1016/j.celrep.2023.113038>.
27. Jacobi, A., Tran, N.M., Yan, W., Benhar, I., Tian, F., Schaffer, R., He, Z., and Sanes, J.R. (2022). Overlapping transcriptional programs promote survival and axonal regeneration of injured retinal ganglion cells. *Neuron* 110, 2625–2645.e7. <https://doi.org/10.1016/j.neuron.2022.06.002>.
28. Li, L., Fang, F., Feng, X., Zhuang, P., Huang, H., Liu, P., Liu, L., Xu, A.Z., Qi, L.S., Cong, L., and Hu, Y. (2022). Single-cell transcriptome analysis of regenerating RGCs reveals potent glaucoma neural repair genes. *Neuron* 110, 2646–2663.e6. <https://doi.org/10.1016/j.neuron.2022.06.022>.
29. Bray, E.R., Yungher, B.J., Levay, K., Ribeiro, M., Dvoryanchikov, G., Ayupe, A.C., Thakor, K., Marks, V., Randolph, M., Danzi, M.C., et al. (2019). Thrombospondin-1 Mediates Axon Regeneration in Retinal Ganglion Cells. *Neuron* 103, 642–657.e7. <https://doi.org/10.1016/j.neuron.2019.05.044>.
30. Wässle, H., and Riemann, H.J. (1978). The mosaic of nerve cells in the mammalian retina. *Proc. R. Soc. Lond. B Biol. Sci.* 200, 441–461. <https://doi.org/10.1098/rspb.1978.0026>.
31. Keeley, P.W., Eglen, S.J., and Reese, B.E. (2020). From random to regular: Variation in the patterning of retinal mosaics. *J. Comp. Neurol.* 532, 2135–2160. <https://doi.org/10.1002/cne.24880>.
32. Bae, J.A., Mu, S., Kim, J.S., Turner, N.L., Tartavull, I., Kemnitz, N., Jordan, C.S., Norton, A.D., Silversmith, W.M., Prentki, R., et al. (2018). Digital Museum of Retinal Ganglion Cells with Dense Anatomy and Physiology. *Cell* 173, 1293–1306.e19. <https://doi.org/10.1016/j.cell.2018.04.040>.
33. Briggman, K.L., Helmstaedter, M., and Denk, W. (2011). Wiring specificity in the direction-selectivity circuit of the retina. *Nature* 471, 183–188. <https://doi.org/10.1038/nature09818>.
34. Bleckert, A., Schwartz, G.W., Turner, M.H., Rieke, F., and Wong, R.O.L. (2014). Visual space is represented by nonmatching topographies of distinct mouse retinal ganglion cell types. *Curr. Biol.* 24, 310–315. <https://doi.org/10.1016/j.cub.2013.12.020>.
35. Heukamp, A.S., Warwick, R.A., and Rivlin-Etzion, M. (2020). Topographic Variations in Retinal Encoding of Visual Space. *Annu. Rev. Vis. Sci.* 6, 237–259. <https://doi.org/10.1146/annurev-vision-121219-081831>.
36. Rousoo, D.L., Qiao, M., Kagan, R.D., Yamagata, M., Palmiter, R.D., and Sanes, J.R. (2016). Two Pairs of ON and OFF Retinal Ganglion Cells Are

- Defined by Intersectional Patterns of Transcription Factor Expression. *Cell Rep.* 15, 1930–1944. <https://doi.org/10.1016/j.celrep.2016.04.069>.
37. Duan, X., Krishnaswamy, A., Laboulaye, M.A., Liu, J., Peng, Y.R., Yamagata, M., Toma, K., and Sanes, J.R. (2018). Cadherin Combinations Recruit Dendrites of Distinct Retinal Neurons to a Shared Interneuronal Scaffold. *Neuron* 99, 1145–1154.e6. <https://doi.org/10.1016/j.neuron.2018.08.019>.
38. Chen, K.H., Boettiger, A.N., Moffitt, J.R., Wang, S., and Zhuang, X. (2015). RNA imaging: Spatially resolved, highly multiplexed RNA profiling in single cells. *Science* 348, aaa6090. <https://doi.org/10.1126/science.aaa6090>.
39. Moffitt, J.R., and Zhuang, X. (2016). RNA Imaging with Multiplexed Error-Robust Fluorescence In Situ Hybridization (MERFISH). *Methods Enzymol.* 572, 1–49. <https://doi.org/10.1016/bs.mie.2016.03.020>.
40. Stringer, C., Wang, T., Michaelos, M., and Pachitariu, M. (2021). Cellpose: a generalist algorithm for cellular segmentation. *Nat. Methods* 18, 100–106. <https://doi.org/10.1038/s41592-020-01018-x>.
41. Wei, W., Hamby, A.M., Zhou, K., and Feller, M.B. (2011). Development of asymmetric inhibition underlying direction selectivity in the retina. *Nature* 469, 402–406. <https://doi.org/10.1038/nature09600>.
42. Jeon, C.J., Strettoi, E., and Masland, R.H. (1998). The major cell populations of the mouse retina. *J. Neurosci.* 18, 8936–8946. <https://doi.org/10.1523/JNEUROSCI.18-21-08936.1998>.
43. Chen, T., and Guestrin, C. (2016). Xgboost: A Scalable Tree Boosting System. Preprint at arXiv. <https://doi.org/10.48550/arXiv.1603.02754>.
44. Benhar, I., Ding, J., Yan, W., Whitney, I.E., Jacobi, A., Sud, M., Burgin, G., Shekhar, K., Tran, N.M., Wang, C., et al. (2023). Temporal single-cell atlas of non-neuronal retinal cells reveals dynamic, coordinated multicellular responses to central nervous system injury. *Nat. Immunol.* 24, 700–713. <https://doi.org/10.1038/s41590-023-01437-w>.
45. Yan, W., Laboulaye, M.A., Tran, N.M., Whitney, I.E., Benhar, I., and Sanes, J.R. (2020). Mouse Retinal Cell Atlas: Molecular Identification of over Sixty Amacrine Cell Types. *J. Neurosci.* 40, 5177–5195. <https://doi.org/10.1523/JNEUROSCI.0471-20.2020>.
46. Choi, J., Li, J., Ferdous, S., Liang, Q., Moffitt, J.R., and Chen, R. (2023). Spatial organization of the mouse retina at single cell resolution by MERFISH. *Nat. Commun.* 14, 4929. <https://doi.org/10.1038/s41467-023-40674-3>.
47. Pérez De Sevilla Müller, L., Shelley, J., and Weiler, R. (2007). Displaced amacrine cells of the mouse retina. *J. Comp. Neurol.* 505, 177–189. <https://doi.org/10.1002/cne.21487>.
48. Hamilton, N.R., Scasny, A.J., and Kolodkin, A.L. (2021). Development of the vertebrate retinal direction-selective circuit. *Dev. Biol.* 477, 273–283. <https://doi.org/10.1016/j.ydbio.2021.06.004>.
49. Wei, W., and Feller, M.B. (2011). Organization and development of direction-selective circuits in the retina. *Trends Neurosci.* 34, 638–645. <https://doi.org/10.1016/j.tins.2011.08.002>.
50. O'Sullivan, M.L., Puñal, V.M., Kerstein, P.C., Brzezinski, J.A.t., Glaser, T., Wright, K.M., and Kay, J.N. (2017). Astrocytes follow ganglion cell axons to establish an angiogenic template during retinal development. *Glia* 65, 1697–1716. <https://doi.org/10.1002/glia.23189>.
51. Ecker, J.L., Dumitrescu, O.N., Wong, K.Y., Alam, N.M., Chen, S.K., LeGates, T., Renna, J.M., Prusky, G.T., Berson, D.M., and Hattar, S. (2010). Melanopsin-expressing retinal ganglion-cell photoreceptors: cellular diversity and role in pattern vision. *Neuron* 67, 49–60. <https://doi.org/10.1016/j.neuron.2010.05.023>.
52. Quattrochi, L.E., Stabio, M.E., Kim, I., Ilardi, M.C., Michelle Fogerson, P., Leyrer, M.L., and Berson, D.M. (2019). The M6 cell: A small-field bistratified photosensitive retinal ganglion cell. *J. Comp. Neurol.* 527, 297–311. <https://doi.org/10.1002/cne.24556>.
53. Krieger, B., Qiao, M., Rousoo, D.L., Sanes, J.R., and Meister, M. (2017). Four alpha ganglion cell types in mouse retina: Function, structure, and molecular signatures. *PLoS One* 12, e0180091. <https://doi.org/10.1371/journal.pone.0180091>.
54. Wu, S.M., and Pang, J.J. (2024). Effects of elevated intraocular pressure on alpha ganglion cells in experimental glaucoma mice. *Vision Res.* 224, 108475. <https://doi.org/10.1016/j.visres.2024.108475>.
55. Bakken, T.E., Hodge, R.D., Miller, J.A., Yao, Z., Nguyen, T.N., Aevermann, B., Barkan, E., Bertagnoli, D., Casper, T., Dee, N., et al. (2018). Single-nucleus and single-cell transcriptomes compared in matched cortical cell types. *PLoS One* 13, e0209648. <https://doi.org/10.1371/journal.pone.0209648>.
56. Ackers-Johnson, M., Tan, W.L.W., and Foo, R.S.Y. (2018). Following hearts, one cell at a time: recent applications of single-cell RNA sequencing to the understanding of heart disease. *Nat. Commun.* 9, 4434. <https://doi.org/10.1038/s41467-018-06894-8>.
57. Do, M.T.H. (2019). Melanopsin and the Intrinsically Photosensitive Retinal Ganglion Cells: Biophysics to Behavior. *Neuron* 104, 205–226. <https://doi.org/10.1016/j.neuron.2019.07.016>.
58. Berry, M.H., Moldavan, M., Garrett, T., Meadows, M., Cravetchi, O., White, E., Leffler, J., von Gersdorff, H., Wright, K.M., Allen, C.N., and Sivy, B. (2023). A melanopsin ganglion cell subtype forms a dorsal retinal mosaic projecting to the supraoptic nucleus. *Nat. Commun.* 14, 1492. <https://doi.org/10.1038/s41467-023-36955-6>.
59. Schmidt, T.M., and Kofuji, P. (2011). Structure and function of bistratified intrinsically photosensitive retinal ganglion cells in the mouse. *J. Comp. Neurol.* 519, 1492–1504. <https://doi.org/10.1002/cne.22579>.
60. Mao, C.A., Li, H., Zhang, Z., Kiyama, T., Panda, S., Hattar, S., Ribelayga, C.P., Mills, S.L., and Wang, S.W. (2014). T-box transcription regulator Tbr2 is essential for the formation and maintenance of Opn4/melanopsin-expressing intrinsically photosensitive retinal ganglion cells. *J. Neurosci.* 34, 13083–13095. <https://doi.org/10.1523/JNEUROSCI.1027-14.2014>.
61. Maloney, R., Quattrochi, L., Yoon, J., Souza, R., and Berson, D. (2024). Efficacy and specificity of melanopsin reporters for retinal ganglion cells. *J. Comp. Neurol.* 532, e25591. <https://doi.org/10.1002/cne.25591>.
62. Berson, D.M., Castrucci, A.M., and Provencio, I. (2010). Morphology and mosaics of melanopsin-expressing retinal ganglion cell types in mice. *J. Comp. Neurol.* 518, 2405–2422. <https://doi.org/10.1002/cne.22381>.
63. Dyer, B., Yu, S.O., Brown, R.L., Lang, R.A., and D'Souza, S.P. (2024). Defining spatial nonuniformities of all ipRGC types using an improved Opn4(cre) recombinase mouse line. *Cell Rep. Methods* 4, 100837. <https://doi.org/10.1016/j.crmeth.2024.100837>.
64. Hughes, S., Watson, T.S., Foster, R.G., Peirson, S.N., and Hankins, M.W. (2013). Nonuniform distribution and spectral tuning of photosensitive retinal ganglion cells of the mouse retina. *Curr. Biol.* 23, 1696–1701. <https://doi.org/10.1016/j.cub.2013.07.010>.
65. Eglen, S.J. (2006). Development of regular cellular spacing in the retina: theoretical models. *Math. Med. Biol.* 23, 79–99. <https://doi.org/10.1093/imammb/dql003>.
66. Roy, S., Jun, N.Y., Davis, E.L., Pearson, J., and Field, G.D. (2021). Inter-mosaic coordination of retinal receptive fields. *Nature* 592, 409–413. <https://doi.org/10.1038/s41586-021-03317-5>.
67. Ahnelt, P.K., Fernández, E., Martínez, O., Bolea, J.A., and Kübber-Heiss, A. (2000). Irregular S-cone mosaics in felid retinas. Spatial interaction with axonless horizontal cells, revealed by cross correlation. *J. Opt. Soc. Am. A Opt. Image Sci. Vis.* 17, 580–588. <https://doi.org/10.1364/josaa.17.000580>.
68. Kay, J.N., Chu, M.W., and Sanes, J.R. (2012). MEGF10 and MEGF11 mediate homotypic interactions required for mosaic spacing of retinal neurons. *Nature* 483, 465–469. <https://doi.org/10.1038/nature10877>.
69. Raven, M.A., Stagg, S.B., and Reese, B.E. (2005). Regularity and packing of the horizontal cell mosaic in different strains of mice. *Vis. Neurosci.* 22, 461–468. <https://doi.org/10.1017/S0952523805224070>.
70. Whitney, I.E., Keeley, P.W., Raven, M.A., and Reese, B.E. (2008). Spatial patterning of cholinergic amacrine cells in the mouse retina. *J. Comp. Neurol.* 508, 1–12. <https://doi.org/10.1002/cne.21630>.

71. Wässle, H., Peichl, L., and Boycott, B.B. (1981). Morphology and topography of on- and off-alpha cells in the cat retina. *Proc. R. Soc. Lond. B Biol. Sci.* 212, 157–175. <https://doi.org/10.1098/rspb.1981.0032>.
72. Wässle, H., Peichl, L., and Boycott, B.B. (1981). Dendritic territories of cat retinal ganglion cells. *Nature* 292, 344–345. <https://doi.org/10.1038/292344a0>.
73. Wong, A.D., Ye, M., Levy, A.F., Rothstein, J.D., Bergles, D.E., and Searson, P.C. (2013). The blood-brain barrier: an engineering perspective. *Front. Neuroeng.* 6, 7. <https://doi.org/10.3389/fneng.2013.00007>.
74. Bose, M., Zhao, M., Toma, K., Ye, X., and Duan, X.A. (2025). neurobiology perspective on the assembly of retinal vasculature from 2D to 3D. *Curr Opin Neurobiol* 93, 103085. <https://doi.org/10.1016/j.conb.2025.103085>.
75. Toma, K., Zhao, M., Zhang, S., Wang, F., Graham, H.K., Zou, J., Modgil, S., Shang, W.H., Tsai, N.Y., Cai, Z., et al. (2024). Perivascular neurons instruct 3D vascular lattice formation via neurovascular contact. *Cell* 187, 2767–2784.e23. <https://doi.org/10.1016/j.cell.2024.04.010>.
76. Dhande, O.S., Estevez, M.E., Quattrochi, L.E., El-Danaf, R.N., Nguyen, P. L., Berson, D.M., and Huberman, A.D. (2013). Genetic dissection of retinal inputs to brainstem nuclei controlling image stabilization. *J. Neurosci.* 33, 17797–17813. <https://doi.org/10.1523/JNEUROSCI.2778-13.2013>.
77. Kay, J.N., De la Huerta, I., Kim, I.J., Zhang, Y., Yamagata, M., Chu, M.W., Meister, M., and Sanes, J.R. (2011). Retinal ganglion cells with distinct directional preferences differ in molecular identity, structure, and central projections. *J. Neurosci.* 31, 7753–7762. <https://doi.org/10.1523/JNEUROSCI.0907-11.2011>.
78. Do, M.T.H., Kang, S.H., Xue, T., Zhong, H., Liao, H.W., Bergles, D.E., and Yau, K.W. (2009). Photon capture and signalling by melanopsin retinal ganglion cells. *Nature* 457, 281–287. <https://doi.org/10.1038/nature07682>.
79. Yan, W., Peng, Y.R., van Zyl, T., Regev, A., Shekhar, K., Juric, D., and Sanes, J.R. (2020). Cell Atlas of The Human Fovea and Peripheral Retina. *Sci. Rep.* 10, 9802. <https://doi.org/10.1038/s41598-020-66092-9>.
80. Aranda, M.L., and Schmidt, T.M. (2021). Diversity of intrinsically photosensitive retinal ganglion cells: circuits and functions. *Cell. Mol. Life Sci.* 78, 889–907. <https://doi.org/10.1007/s00118-020-03641-5>.
81. Wang, A.Y.M., Kulkarni, M.M., McLaughlin, A.J., Gayet, J., Smith, B.E., Haupschein, M., McHugh, C.F., Yao, Y.Y., and Puthussery, T. (2023). An ON-type direction-selective ganglion cell in primate retina. *Nature* 623, 381–386. <https://doi.org/10.1038/s41586-023-06659-4>.
82. Lu, Y., Shiau, F., Yi, W., Lu, S., Wu, Q., Pearson, J.D., Kallman, A., Zhong, S., Hoang, T., Zuo, Z., et al. (2020). Single-Cell Analysis of Human Retina Identifies Evolutionarily Conserved and Species-Specific Mechanisms Controlling Development. *Dev. Cell* 53, 473–491.e9. <https://doi.org/10.1016/j.devcel.2020.04.009>.
83. Lilley, B.N., Sabbah, S., Hunyara, J.L., Gribble, K.D., Al-Khindi, T., Xiong, J., Wu, Z., Berson, D.M., and Kolodkin, A.L. (2019). Genetic access to neurons in the accessory optic system reveals a role for Sema6A in midbrain circuitry mediating motion perception. *J. Comp. Neurol.* 527, 282–296. <https://doi.org/10.1002/cne.24507>.
84. Zhang, J., Li, L., Huang, H., Fang, F., Webber, H.C., Zhuang, P., Liu, L., Dalal, R., Tang, P.H., Mahajan, V.B., et al. (2019). Silicone oil-induced ocular hypertension and glaucomatous neurodegeneration in mouse. *eLife* 8, e45881. <https://doi.org/10.7554/eLife.45881>.
85. Fang, F., Zhang, J., Zhuang, P., Liu, P., Li, L., Huang, H., Webber, H.C., Xu, Y., Liu, L., Dalal, R., et al. (2021). Chronic mild and acute severe glaucomatous neurodegeneration derived from silicone oil-induced ocular hypertension. *Sci. Rep.* 11, 9052. <https://doi.org/10.1038/s41598-021-88690-x>.
86. Williams, P.R., Benowitz, L.I., Goldberg, J.L., and He, Z. (2020). Axon Regeneration in the Mammalian Optic Nerve. *Annu. Rev. Vis. Sci.* 6, 195–213. <https://doi.org/10.1146/annurev-vision-022720-094953>.
87. Choi, J., Li, J., Ferdous, S., Liang, Q., Moffitt, J.R., and Chen, R. (2023). Author Correction: Spatial organization of the mouse retina at single cell resolution by MERFISH. *Nat. Commun.* 14, 6057. <https://doi.org/10.1038/s41467-023-41825-2>.
88. Wang, X., Allen, W.E., Wright, M.A., Sylwestrak, E.L., Samusik, N., Vesuna, S., Evans, K., Liu, C., Ramakrishnan, C., Liu, J., et al. (2018). Three-dimensional intact-tissue sequencing of single-cell transcriptional states. *Science* 361, eaat5691. <https://doi.org/10.1126/science.aat5691>.
89. Han, L., Liu, Z., Jing, Z., Liu, Y., Peng, Y., Chang, H., Lei, J., Wang, K., Xu, Y., Liu, W., et al. (2025). Single-cell spatial transcriptomic atlas of the whole mouse brain. *Neuron* 13, 2141–2160.e9. <https://doi.org/10.1016/j.neuron.2025.02.015>.
90. Sousa, V.H., Miyoshi, G., Hjerling-Leffler, J., Karayannis, T., and Fishell, G. (2009). Characterization of Nkx6-2-derived neocortical interneuron lineages. *Cereb. Cortex* 19, i1–i10. <https://doi.org/10.1093/cercor/bhp038>.
91. Wolf, F.A., Angerer, P., and Theis, F.J. (2018). SCANPY: large-scale single-cell gene expression data analysis. *Genome Biol.* 19, 15. <https://doi.org/10.1186/s13059-017-1382-0>.
92. Matcham, A.C., Toma, K., Tsai, N.Y., Sze, C.J., Lin, P.Y., Stewart, I.F., and Duan, X. (2024). Cadherin-13 Maintains Retinotectal Synapses via Transneuronal Interactions. *J. Neurosci.* 44, e1310232023. <https://doi.org/10.1523/JNEUROSCI.1310-23.2023>.
93. Pachitariu, M., and Stringer, C. (2022). Cellpose 2.0: how to train your own model. *Nat. Methods* 19, 1634–1641. <https://doi.org/10.1038/s41592-022-01663-4>.
94. Traag, V.A., Waltman, L., and van Eck, N.J. (2019). From Louvain to Leiden: guaranteeing well-connected communities. *Sci. Rep.* 9, 5233. <https://doi.org/10.1038/s41598-019-41695-z>.
95. Zhang, M., Eichhorn, S.W., Zingg, B., Yao, Z., Cotter, K., Zeng, H., Dong, H., and Zhuang, X. (2021). Spatially resolved cell atlas of the mouse primary motor cortex by MERFISH. *Nature* 598, 137–143. <https://doi.org/10.1038/s41586-021-03705-x>.

## STAR★METHODS

### KEY RESOURCES TABLE

REAGENT or RESOURCE	SOURCE	IDENTIFIER
<b>Antibodies</b>		
Goat anti-Spp1 (Osteopontin)	R&D Systems	Cat#AF808; RRID: AB_2194992
Rabbit anti-Tbx20	Boster Bio	Cat#A04704
Rabbit anti-mouse Opn4	ATSBio	Cat#AB-N38; RRID: AB_1608077
Chicken anti-GFP	Abcam	Cat#ab13970; RRID: AB_300798
Rabbit anti-RFP	Rockland	Cat#600-401-379; RRID: AB_2209751
Rabbit anti-RBPMS	Proteintech	Cat#15187-1-AP; RRID: AB_2238431
Rabbit anti-Cartpt	Phoenix Pharmaceuticals	Cat#H-003-62; RRID: AB_2313614
Mouse anti-Tuj1	Biolegend	Cat#801201; RRID: AB_2728521
Rat anti-mouse CD31	BD Pharmingen	Cat#550274; RRID: AB_393571
Mouse anti-human CD31 (PECAM)	BD Biosciences	Cat#555444; RRID: AB_395837
Goat anti-vAChT	Promega	Cat#G4481; RRID: AB_430859
Goat anti-GFP	Rockland	Cat# 600-101-215; RRID: AB_218182
<b>Chemicals, peptides, and recombinant proteins</b>		
32% Paraformaldehyde (Formaldehyde) Solution	EMS	15714
Ammonium Persulfate	Millipore-Sigma	09913-100G
Ethyl Alcohol, Pure (200 proof) Koptec	Thomas Scientific	C961Y20
N, N,N', N'-Tetramethylethylenediamine (TEMED)	Millipore-Sigma	T7024-25ML
RNase Inhibitor, Murine	NEB	M0314L
Proteinase K, Molecular Biology Grade	NEB	P8107S
Phosphate buffered saline (10X) pH 7.4, RNase-free	Thermo Fisher	AM9625
UltraPure DNase/RNase-free Distilled Water	Thermo Fisher	10977015
D-Sucrose 99.9% DNase-, RNase- and Protease-Free	Fisher Scientific	BP2201
TSA Vivid 650	Biotechne	323273
Opal 570	Akoya Bioscience	FP1488001KT
Opal 690	Akoya Bioscience	FP1497001KT
<b>Critical commercial assays</b>		
MERSCOPE Slide	Vizgen	20400001
MERSCOPE Sample Prep Kit	Vizgen	10400012
MERSCOPE 140 Gene Panel for mouse RGCs	Vizgen	VZG179
MERSCOPE Cell Boundary Stain Kit	Vizgen	10400118
MERSCOPE 140 Gene Imaging Kit	Vizgen	10400004
MERSCOPE Anti-Rat Protein Stain Kit	Vizgen	10400109
MERSCOPE Anti-Goat Protein Stain Kit	Vizgen	10400108
MERSCOPE Anti-Rabbit Protein Stain Kit	Vizgen	10400107
Human-RBPMS-C2	ACD Bio	554451-C2
Human-CD31 (PECAM)-O1-C3	ACD Bio	487381-C3
Human-OPN4-C2	ACD Bio	504991-C2
Human-BNC2-C1	ACD Bio	496801
Human-FOXP2-C3	ACD Bio	407261-C3
Mouse-Fam19a4-C2	ACD Bio	495021-C2
Mouse-Cdh6-C2	ACD Bio	519541-C2
Mouse-Gpr88-C3	ACD Bio	31745-C3
Mouse-Tbx20-C2	ACD Bio	511991-C2

(Continued on next page)

**Continued**

REAGENT or RESOURCE	SOURCE	IDENTIFIER
Mouse-Serpine-C2	ACD Bio	435241-C2
Mouse-Opn4-C1	ACD Bio	438061-C1
Mouse-Opn4-C2	ACD Bio	438061-C2
Mouse-Nmb-C3	ACD Bio	459931-C3
RNAscope Multiplex Fluorescent Detection Kit v2	ACD Bio	Cat#323110
<b>Deposited data</b>		
Final data files for MERFISH analysis	This manuscript	Zenodo: <a href="https://doi.org/10.5281/zenodo.16342107">https://doi.org/10.5281/zenodo.16342107</a>
Raw matrices for MERFISH analysis	This manuscript	GEO: GSE303399
<b>Experimental models: Organisms/strains</b>		
Mouse: C57BL/6J wildtype	Jackson Laboratory	Cat# 000664; RRID: IMSR_JAX:000664
Mouse: Opn4-Cre	Jackson Laboratory	Cat# 035925; RRID: IMSR_JAX:035925
Mouse: Kcng4-Cre	Jackson Laboratory	Cat# 029414; RRID: IMSR_JAX:029414
Mouse: Foxp2-Cre	Jackson Laboratory	Cat# 030541; RRID: IMSR_JAX:03054
Mouse: Opn4:tdTomato (BAC transgenic)	Gift from K.W Yau	Do et al. <sup>78</sup>
Mouse: Hoxd10-GFP (BAC Transgenic)	Gift from S. Varadarajan	Dhande et al. <sup>76</sup>
Mouse: Hb9-GFP	Jackson Laboratory	Cat# 005029; RRID: IMSR_JAX:005029
Mouse: Nts-Cre	Jackson Laboratory	Cat#017525; RRID: IMSR_JAX:017525
Mouse: Rosa26-CAG-Lox-Stop-Lox (LSL)-GFP	Gift of G. Fishell	Sousa et al. <sup>90</sup>
<b>Software and algorithms</b>		
Fiji	<a href="https://fiji.sc">https://fiji.sc</a>	RRID: SCR_002285
Computational scripts detailing MERFISH analysis	This manuscript	Zenodo: <a href="https://doi.org/10.5281/zenodo.16369976">https://doi.org/10.5281/zenodo.16369976</a>
Cellpose	<a href="http://www.cellpose.org/">http://www.cellpose.org/</a>	RRID: SCR_021716
Jupyter Notebook	<a href="https://jupyter.org/">https://jupyter.org/</a>	Jupyter Notebook
Imaris	<a href="http://www.bitplane.com/imiris">http://www.bitplane.com/imiris</a>	RRID: SCR_007370
Scanpy	Wolf et al. <sup>91</sup>	RRID:SCR_018139
OpenCV	<a href="https://opencv.org/">https://opencv.org/</a>	RRID: SCR_015526
<b>Other</b>		
MF-Millipore™ Membrane Filter, 0.45 µm pore size, gridded, 13 mm diameter, mixed cellulose esters (MCE) membrane, hydrophilic, black, 100 discs	Millipore	HABG01300
Polysciences, Inc. Mold, Peel-A-Way Embedding Molds	VWR	NC9991740
EMS Tissue Freezing Medium	EMS	72592

## EXPERIMENTAL MODEL AND STUDY PARTICIPANT DETAILS

### Genetically modified mouse lines for RGC subset labeling

All animal experiments were approved by the Institutional Animal Care and Use Committees (IACUC) at the University of California at San Francisco. Mice were maintained under regular housing conditions with standard access to water and food in a pathogen-free facility. Male and female mice were used in equal numbers; no sexual dimorphisms were observed in retinal neuron development or vascular development, and all ages and numbers were documented. Genotypes were determined by PCR from toe or tail biopsy. Littermates were used for genetic comparison, as indicated in experimental details. Dates of birth were tracked following the vivarium birth notice and cross-referenced by JAX guidelines. Specifically, the following mouse lines were used in the following categories:

1. RGC marker lines include the following: Hb9-GFP transgenic mice express EGFP in ventral-preferring On-Off DSGCs.<sup>37</sup> This transgenic line has been well characterized to mark On-Off DSGCs that are Cartpt-positive.

2. Kcng4-Cre; Lox-Stop-Lox (LSL)-GFP mark all  $\alpha$ RGCs,<sup>10,25</sup> including C43 (M4 ipRGC, On-Sustained), C45 (Off-transient), and C42 (Off-sustained) characterized here.
3. Opn4-Cre; LSL-GFP mark M1-M6 ipRGCs,<sup>51,61</sup> including M1 (C40, C33), M2 (C31), M4 (C43) and M5 (C21) ipRGCs characterized in this study. No significant M3 or M6 ipRGCs from this line were detected in the current MERFISH-based platform, which is expected given their sparseness and morphological heterogeneity.<sup>59,62</sup>
4. Opn4-TdTomato<sup>78</sup> were observed to primarily mark M1 and M2 ipRGCs (C40, C33, and C31). The Opn4-TdTomato BAC transgenic line was a gift from K.W. Yau (Hopkins).
5. Hoxd10-GFP label On-DSGC subsets (C10) and a fraction of Temporal On-Off DSGCs, which are Cartpt-negative.<sup>76</sup> We further characterized this transgenic line using molecular markers based on scRNA-seq, as shown in Figures S6A–S6D. The Hoxd10-GFP BAC transgenic line was a gift from S. Varadarajan (Univ Texas Southwestern Med).
6. Nts-Cre; LSL-GFP marks RGCs expressing Neurotensin (Nts), which were previously characterized to be perivascularly enriched.<sup>75</sup>
7. Foxp2-Cre;LSL-GFP marks RGCs in a subset of Foxp2-expressing retinal ganglion cells (F-RGCs).<sup>36</sup>
8. Wildtype C57/Bl6J mice were used to carry out the set of MERFISH experiments to establish the atlas.

### Human retinal tissues

For prenatal human retina tissue collection, protocols (10-05113) were approved by the Human Gamete, Embryo, and Stem Cell Research Committee at UCSF. De-identified second-trimester human tissue samples were collected with previous patient consent in strict observance of the legal and institutional ethical regulations. Human eye tissues were processed as previously described in Zhao et al.<sup>26</sup> They were harvested from eye enucleations, followed by 4% PFA fixation at 4°C overnight. Retinal tissues were removed and embedded for long-term storage and subsequent processing. GW22-23 samples were primarily used in the current study. Prenatal macular tissues were dissected into smaller ~25 mm<sup>2</sup> pieces, similar to the mouse histology. This region contains active angiogenesis during development and also contains multiple layers of RGCs. The vasculature in the macular region extended into the bottom layer of the RGCs. RNA *in situ* hybridization and immunohistochemistry were carried out using the protocols established above.

### METHOD DETAILS

#### Mouse retinal wholemount sectioning

To track the orientation of the retina during the flatmount preparation, the nasal side of each mouse eye was marked with a marker pen as previously described in Wei et al.<sup>41</sup> Such an orientation registering on the nasal side is consistent across all MERFISH experiments as well as experimental validations, as detailed in Figures 2, 4, and S1. The entire globe was subsequently fixed in 4%PFA on ice for 30 min, dissected to remove the cornea and lens, and then placed back into 4%PFA on ice for another 30 min. The sclera was peeled off from the retina, and radial cuts were made to allow for flattening and orientation marking. The retina was then transferred to RNA-grade 30% sucrose/PBS and kept at 4°C until it sank. Once equilibrated, the retina was mounted onto a membrane filter (MF-Millipore). The retina and filter paper then underwent two cycles of drying and rewetting and 30% sucrose/PBS, followed by 5 min of drying. The membrane filter was trimmed to be slightly larger than the size of the retina, and the filter paper with the retina was adhered to a flat stage made from tissue-freezing medium (EMS), mounted on a cryostat chuck. The retina was embedded in a thin layer of tissue-freezing medium, and the chuck was placed on a block of dry ice to solidify the tissue-freezing medium. The embedded retina was stored overnight at -80°C. Before sectioning, the retina block was equilibrated within the cryostat. Care was taken to maintain the flat orientation of the tissue while trimming and sectioning the block. Sections of 12 $\mu$ m thickness were collected onto MERSCOPE slides (Vizgen). Each slide was washed with DEPC-treated PBS and incubated in 70% ethanol at 4°C overnight to permeabilize the tissue. Samples were then either processed for MERFISH imaging or stored in 70% ethanol as flatmount slides at 4°C for up to 1 month.

#### MERFISH workflow using MERSCOPE

The samples on MERSCOPE slides (Vizgen) were dehydrated through an ethanol series: 90% EtOH at Room Temperature (RT) for 5 min, 100% EtOH at RT for 1 h, 90% EtOH at RT for 5min, and incubated with 70% EtOH at RT for 5 min. Retinal sections were then prepared for MERSCOPE imaging following Vizgen protocols for fixed frozen tissue, including the following steps as detailed in the MERSCOPE sample prep protocol:

First, Cell Boundary Staining and Protein Staining: The sample was washed with 5 mL of PBS. Blocking solution (10:1 Blocking Buffer C Premix: RNase inhibitor) was then added to the center of the tissue section and incubated at RT for 1 h. The sample was incubated in Primary Staining Solution (100:10:1 Blocking Buffer C Premix: RNase inhibitor: Primary antibody) at RT for 1 h. The sample was subsequently washed with 1XPBS. Secondary Staining Solution (100:10:3:1 Blocking Buffer Premix: RNase inhibitor: Cell Boundary Secondary Stain Mix: Protein Stain) was then added to the sample and incubated for 1 h. Subsequently, the sample was washed with PBS. Fixation Buffer (4% PFA in PBS) was then added to the tissue section and incubated at RT for 15 min. The sample was then washed with PBS. In this case, we also applied the Cell boundary staining (Vizgen) for cell segmentation, as the cells within the GCL are closely packed within a monolayer, precluding DAPI and RNA-transcript-based imaging segmentation

methods. (Cell Boundary #2 Channel) most clearly delineated cell boundaries in the mouse GCL and, therefore, was used for segmentation.

Second, Optimized immunohistochemistry protocols in parallel to RNA transcript detection: A set of RNAase-free antibodies was first validated, including anti-GFP (Goat), anti-Melanopsin (Rabbit), anti-Spp1 (Goat), and anti-mouse-CD31 (Rat) that were used in the current MERFISH preparation. Antibody dilutions were optimized for MERFISH experiments to ensure signal detection. Respective antibody staining kits for different species (Rat, Rabbit, Goat) were utilized accordingly and assigned to distinct imaging channels in parallel to MERFISH transcript channels.

Third, Encoding Probe Hybridization: The sample was incubated in 5 mL Formamide Wash Buffer at 37°C for 30 min. The Formamide Wash Buffer was then carefully aspirated, and the custom 140-Gene MERSCOPE Gene Panel Mix (Vizgen, VZG179) was added to the tissue section and incubated in a humidified chamber at 37°C for at least 36 h and a maximum of 48 h. Then, in the post Encoding Probe Hybridization washes, Formamide Wash Buffer was added to the sample and incubated at 47°C for 30 min. This wash step was repeated, followed by incubating the sample in Sample Prep Wash Buffer for 2 min.

Fourth, Gel Embedding: the Sample Preparation Wash Buffer was aspirated from the MERSCOPE slide, and Gel Embedding Solution (2:10:1 Gel Embedding Premix:10% w/v ammonium persulfate solution:N,N,N',N'-tetramethylethylenediamine) was added to cover the tissue sections. A coverslip pretreated with Gel Slick was placed directly over the tissue sections and incubated at RT for 90 min to solidify the gel. The coverslip was then removed. Then, the sample was treated for clearing. The sample was incubated in a pre-warmed Clearing Solution (100:1 Clearing Premix: Proteinase K) at 47°C for 24 h.

Fifth, DAPI and PolyT staining: Following the removal of the Clearing Solution, the sample was washed with a Sample Prep Wash Buffer. DAPI and PolyT Staining Reagent were then added to the sample and incubated at RT for 15 min on a rocker. This was followed by washing with Formamide Wash Buffer for 10 min and 5 mL Sample Prep Wash Buffer.

Last, MERFISH imaging: The sample was loaded on the MERSCOPE machine for imaging, which automates the MERFISH probe exchange and readout process.

As a technical note, the MERFISH protocols require multiple high-salt washes over 3–5 days, which inevitably causes random tissue loss—a limitation reported in prior MERFISH studies of brain tissue. In section-based work (e.g., Choi et al.<sup>87</sup>), such loss is masked by discarding damaged slices, but it becomes obvious when the goal, as here, is complete coverage of the whole retina. Crucially, the missing areas in our samples are scattered rather than confined to the same region in every specimen. Although random loss limits claims about exact gradients or absolute densities at the extreme periphery, we restrict our claims on topography to “broad” D/V and N/T biases.

### Mouse retina immunohistochemistry

Mouse eyes were collected and fixed in 4% PFA/PBS on ice for 30 min, followed by retina dissection, post-fixation for 30 min, and rinsing with PBS. Retinas were analyzed as cryosections and flatmounts as previously described in Duan et al.<sup>15</sup> Wholemount retina samples were incubated with blocking buffer (5% normal donkey serum, 0.5% Triton-X-100 in PBS) overnight, then incubated for 2–4 days at 4°C with primary antibodies. For sectioning, fixed retinas were incubated in 30% sucrose in PBS for 2 h, then frozen in OCT as blocks and sectioned at 20 µm. Vertical sections were incubated with 0.3% Triton X-100 and 3% donkey serum in PBS for 1 h, followed by overnight incubation with primary antibodies at 4°C. Secondary antibodies were then applied for 2 h at room temperature. Retinas or sections were mounted onto glass slides using SlowFade Gold antifade reagent (Invitrogen). The following immunohistochemistry antibodies used were as follows: rabbit and chicken anti-GFP (1:1000, Millipore; 1:500, Abcam); goat anti-VACHT (1:500, Promega); rabbit anti-Cartpt (1:2500, Phoenix Pharmaceuticals); rabbit anti-Opn4 (1:1000, ATSBio); goat anti-Osteopontin/Spp1 (1:500, R&D Systems); mouse anti-Tuj1 (1:1000, Biologen); rabbit anti-RBPMS (1:1000, Proteintech); rat anti-mouse CD31 (1:100, BD Biosciences); mouse anti-human CD31 (1:100, BD Biosciences). The primary antibodies were detected with Alexa Fluor Dye-conjugated secondary antibodies (Invitrogen). Nuclei were stained with DAPI.

### Retinal RNAscope *in situ* hybridization

*In situ* hybridization on retina sections was performed primarily using RNAscope Multiplex Fluorescent Detection Kit V2 (ACD Bio), as previously described in Matcham et al.<sup>92</sup> The retina sections were post-fixed in 4% PFA and washed in PBS. After target retrieval, the sections were treated with Protease III, incubated with target probes, and then treated with amplification reagents. They were subsequently developed using TSA Fluorescein, Cy3, and Cy5 fluorophores (Akoya Bioscience). For GFP-guided marker analysis, GFP detection by immunohistochemistry was performed after RNAscope detection. An optimized *in situ*-based GFP antibody (chicken anti-GFP, Aves Biosciences) was used for RNAscope-IHC double detection. Slides were mounted using SlowFade Gold antifade reagent (Invitrogen). RNAscope Probes included the following: RNAscope Probes: Mm-Fam19a4-C2 (495021-C2); Mm-Gpr88-C3 (317451-C3); Mm-Cdh6-C2 (519541-C2). RNAscope Probe-Hs-PECAM1(CD31)-O1-C3 (487381-C3); RNAscope Probe-Hs-RBPMS-C2 (554451-C2); Human-OPN4-C2(504991-C2); Human-BNC2-C1 (496801); Human-FOXP2-C3(407261-C3).

*In situ* hybridization on a retina whole mount was performed using the RNAscope Multiplex Fluorescent Detection Kit v2 (ACDBio) and the probes described above. We slightly modified the protocols to adapt the reagents to wholemount. Mouse Opn4 mRNA was labeled using Opal 570 (Akoya Bioscience), and Nmb mRNA was labeled using TSA Vivid 650 or Opal 690 fluorophores. All retinas were imaged on a Leica SP8 microscope at 20X magnification. Nmb-positive RGCs were counted in ImageJ/FIJI.

### No-pupillary dilation silicone oil induced ocular hypertension under-detected model (ND SOHU)

ND SOHU was induced in wild-type animals or mouse transgenic lines using methods described in Fang et al.<sup>85</sup> In brief, the intraocular pressure of both mouse eyes was measured prior to the procedure. The cornea was punctured with a 32G needle from the superior temporal side (approximately 0.5 mm from the limbus); the needle penetrated about 0.3 mm, avoiding damage to the lens or iris. Then, a glass microelectrode prefilled with silicone oil (SO, 1,000 mPa s, Silikon, Alcon Laboratories) was inserted through the same corneal tunnel to inject SO into the anterior chamber until droplets covered most of the iris surface. The corneal incision was closed by gently pushing the upper eyelid of the mouse. For each ND SOHU-treated animal included in the dataset, we utilized the following criteria: the IOP was within the range of (24 ± 10 mmHg) over 3 weeks of treatment; 3 weeks of ND SOHU treatment consistently resulted in ~45% survival of the RGCs as an internal control (RBPMs-positive; Figure 6E); photoreceptor layers stayed largely intact after glaucomatous conditions to avoid secondary effects of ischemic conditions, potentially caused by hyper-elevated IOP; control eyes were devoid of any deficits and variability due to genetics.

### Optic nerve crush (ONC) model

ONC procedures were carried out as previously described in Duan et al.<sup>25</sup> In brief, a mouse was first anesthetized, followed by a peritomy on the eye, created by incising the conjunctiva at approximately the 4 o'clock position using a pair of spring scissors. A gentle dissection was used to bring the optic nerve into view as it exited the globe. A crush injury to the optic nerve was then made using a pair of forceps at about 2 mm from the globe for 5 s, followed by post-op care. Contralateral eyes were used for sham control in the same animal.

## QUANTIFICATION AND STATISTICAL ANALYSIS

### Gene panel simulation

To evaluate the number of genes required for RGC classification, we used three approaches as listed below.

In the first approach, we identified a fixed number of differentially expressed genes for each RGC type. We began by considering all pairs of a single cluster  $i$  and a single gene  $j$  in the scRNA-seq atlas of adult RGCs. Next, we removed pairs wherein fewer than 40% of cells in the cluster expressed the corresponding gene. For each remaining cluster-gene ( $i,j$ ) pair, we calculated a specificity score  $s_{i,j}$

$$s_{i,j} = \log_2 \frac{p_{i,j} + \gamma}{p_{i,j}^{\text{rest}} + \gamma}$$

where  $p_{i,j}$  is the proportion of cluster  $i$  cells expressing gene  $j$ ,  $p_{i,j}^{\text{rest}}$  is the proportion of all remaining cells expressing gene  $j$ , and  $\gamma = 0.02$  is a pseudocount. For each cluster  $i$ , we then picked the genes corresponding to the top  $k$  specificity scores, resulting in a gene panel of size  $45*k$ , encompassing all 45 RGC types. Note that while a gene can be selected for more than one cluster, this did not occur in our case. We constructed gene panels corresponding to  $k = 1, 2, 3$ , and 4.

In the second approach, we randomly sampled 140 genes from the full set of ~18k genes expressed in the data, repeating this  $n = 10$  times to estimate variance. This random gene set served as a baseline.

Finally, in the third approach, we randomly sampled 140 genes from the set of 2000 highly variable genes (as selected by 'Seurat\_v3', implemented in `scipy.stats.hv_genes`). As in the second approach, we repeated this  $n = 10$  times.

### Preprocessing MERFISH data

For each 12 μm tissue section, the MERFISH protocol generated eight 1.5 μm optical sections ( $z_0, z_1, \dots, z_7$ ), spanning the ganglion cell layer (GCL) to the inner plexiform layer (IPL) along the retina's depth. Due to the large image sizes, each optical section was scaled to be 4 times smaller along both the length and width (as implemented by OpenCV's `cv2.resize` function). Each optical section was then segmented using a fine-tuned *Cellpose* model<sup>93</sup> based on the pre-trained "cyto2" algorithm. Fine-tuning was performed on sixteen manually annotated regions, each containing 50–200 soma, to improve segmentation accuracy for somas with darker staining or significantly smaller or larger soma sizes than average within the sample. The fine-tuned model used the following hyperparameters: 'mask\_threshold'=0.4, 'flow\_threshold'=0.4, and a diameter of 22 (pixels), with the other parameters set to default. Additionally, rare instances of tissue regions containing only non-RGC neurons (e.g., amacrine cells, Müller glia, and bipolar cells) from the inner nuclear layer, inadvertently included during sectioning, were manually excluded from downstream analysis.

Adjacent optical sections were stitched together by assessing pixel overlap between segmented cells across consecutive optical sections. Overlap was measured using the Jaccard Index (intersection over union) between cell regions in two adjacent optical sections  $z_i$  and  $z_{i+1}$ . A cell from  $z_{i+1}$  was assigned to a cell in  $z_i$  if the Jaccard index exceeded 0.15. In case of multiple cells exceeding this threshold, we picked the one with the highest overlap. Cells without sufficient overlap were treated as distinct. This stitching approach accommodates the fact that many GCL somas are <12 μm in diameter and thus span only part of an optical section. Transcripts were then registered to segmentation masks according to their pixel locations, generating a cell-by-gene matrix for each tissue section. To estimate soma volumes, we took the largest cross-sectional area of each cell across all optical sections, calculated an equivalent radius, and derived the corresponding sphere volume. We also tested a maximum-intensity Z-projection followed by segmentation, but overlapping somas in the projection distorted boundaries, making this approach unreliable. Instead, we fine-tuned *Cellpose*'s 'cyto2' model with 5 regions of interest (containing ~150 manually labeled cells), which significantly improved the

detection of darkly stained cells and small somas. After segmentation and stitching, tissue sections were manually aligned using DAPI-stained optical sections via rotational and translational adjustments.

For each retina, cells with fewer than 15 transcripts were excluded, and those with more than 2 transcripts of *Chat*, *Tfap2a*, or *Tfap2b* were labeled as expressing amacrine cell (ACs) markers. Cells meeting neither of these criteria but with more than 10 transcripts of RGC markers (*Rbpms*, *Slc17a1*, *Pou4f1*, *Pou4f2*, or *Slc17a6*) were considered to express RGC markers. Clustering was performed using the Leiden algorithm in Scanpy,<sup>94</sup> and clusters were annotated as RGCs or dACs based on their dominant marker expression. About 15% of cells could not be definitively annotated and consisted of non-neuronal cells (NNs) and low-quality cells (see below).

### GCL cell class verification via XGBoost

To verify cell class assignments, an XGBoost classifier<sup>43</sup> was trained on published scRNA-seq datasets encompassing all retinal cell classes.<sup>12,44,45</sup> Using the 130 genes that comprised the MERFISH panel (i.e., excluding the 9 failed probes in Figure S2D and 1 probe that was incorrectly picked during panel design), raw counts were normalized in each cell to the median value across all cells, followed by log-transformation and scaling to unit variance and zero mean. The classifier used a multiclass soft probability objective function with log-loss evaluation, 200 boosting rounds, a maximum tree depth of 4, a 40% subsampling rate, and a learning rate of 0.2. We used 30% of the dataset for validating the classifier, with rare RGC types (<100 cells) upsampled to 100 cells and highly abundant types (>2000 cells) randomly downsampled to 2000 cells to form the training set. Cells with classification probabilities >0.5 were deterministically assigned to a type; others were marked as unassigned. The validation accuracy of this model and concordance with MERFISH clustering are displayed in Figures 3B and S1A–S1C. In particular, the model's predictions were used to annotate non-neuronal cells.

### RGC classification

RGC types in MERFISH data were identified by classifying cells using an XGBoost model trained on the reference RGC scRNA-seq atlas alone. The XGBoost hyper-parameters, training and validation procedure, and assignment thresholds are the same as described above.

### RGC spatial distributions in the 2D space

For each RGC type  $i$ , we calculated spatial bias scores along the D/V (Dorsal/Ventral) and T/N (Temporal/Nasal) axes. The D/V bias score is:

$$\text{Score}(i)_{D/V} = \log_2 \frac{p_{i,D}}{p_{i,V}}$$

where  $p_{i,D}$  and  $p_{i,V}$  are the proportions of somas of RGC type  $i$  in the dorsal and ventral regions of the retina, respectively. The expression for the T/N bias score is analogous. Welch's t tests with Benjamini-Hochberg corrections were used to identify significant spatial biases, evaluating the null hypothesis that  $\text{Score}(i)_{D/V} = \text{Score}(i)_{T/N} = 0$ .

### Perivascularity of RGC types

To assess whether specific RGC types concentrate near retinal blood vessels, we adapted a permutation test described in a previous study in Zhang et al.<sup>95</sup> Briefly, we computed a nearest-neighbor graph ( $n = 15$ ) connecting non-neuronal cells and RGCs, with edges removed if they were greater than 25  $\mu\text{m}$  away (to account for edge effects and holes in the retina). RGC-type labels were shuffled within the same tissue section and quadrant to generate null distributions, leaving the vessel locations intact. To minimize potential global biases in the distribution, we only allowed labels to be permuted between RGCs in the same tissue section, as well as the same quadrant of the retina. We then calculated a Z score between each cell type pair  $(i, j)$  for a given tissue section quadrant  $q$ , as follows:

$$z_{ij}^q = \frac{x_{ij}^q - \mu_{ij}^q}{\sigma_{ij}^q}$$

Where  $x_{ij}^q$  is the observed edge count between cell types  $i$  and  $j$  in the quadrant  $q$ ,  $\mu_{ij}^q$  is the mean number of total edges between cell types  $i$  and  $j$  in the quadrant  $q$  averaged across 1000 permutations, and  $\sigma_{ij}^q$  is the standard deviation of the total number of edges between cell types  $i$  and  $j$  in quadrant  $q$  averaged across 1000 permutations. Z scores were aggregated across quadrants using Stouffer's method.

$$z_{ij} = \frac{\sum_{q=1}^n z_{ij}^q}{\sqrt{n}}$$

and the  $z_{ij}$  were used to calculate two-sided  $p$  values  $p_{ij}$ , under the assumption of normality

$$p_{ij} = 2(1 - F(z_{ij}))$$

where  $F$  is the cumulative distribution function of the standard normal distribution. The nominal  $p$  values  $p_{ij}$  were adjusted using the Benjamini-Hochberg procedure.

Density heatmaps for each type are calculated as follows. First, cells from each retina are manually aligned to the same coordinate system ( $x = 0, y = 0$  is the center for each retina). Cells are assigned to discretized spatial bins of size approximately  $40 \mu\text{m} \times 40 \mu\text{m}$  each, with  $101 \times 101$  bins total. For a given type in a given bin, a density is calculated as the number of cells of a given type in a bin divided by the total number of cells in the bin. Secondly, the relative densities for a given type are then smoothed via a Gaussian with kernel size of  $(41, 41)$  and  $\sigma_x = \sigma_y = 15$  (implemented with `cv2.GaussianBlur`). ‘0’ is defined as the minimum value across bins, and ‘1’ is the maximum value across bins, with all bin values being linearly scaled accordingly.

### Local spatial analysis of each RGC type

Due to the nature of the stitched segmentation, cells may overlap along the  $z$  axis, albeit infrequently in our experience ( $\sim 10\%-15\%$  of cells), and with a median overlap of 5% in area. While this has little impact on cell type classification and the analysis of broad topographic biases, overlaps can impact the values of regularity indices. Therefore, for analyses of intersomal spacing at the cell type level, we adjusted our segmentation to be 2D to better match previous work,<sup>31</sup> which assumes soma are not allowed to overlap. To do this, we repeated the stitching process, going one optical section at a time ( $z_7, z_6, \dots, z_0$ ), and only adding new cells that had no overlap along the  $x$ - $y$  plane with a previously added cell. This resulted in a new segmentation we refer to as the 2D-refined segmentation. The new segmentation approach yields a loss of 10%-15% of cells. In principle, these could be recovered using more advanced approaches that apply dilational transforms to avoid soma overlap, but as approaches possess their own arbitrariness, we do not use them here.

We calculated the nearest neighbor regularity index (NNRI) for each RGC type.<sup>31,71,72</sup> Within each ROI  $r$ , we calculated the distance of each RGC to the nearest neighbor of the same type  $i$ . The NNRI statistic for the observed distributions was calculated as

$$\text{NNRI}_{r,i}^{\text{obs}} = \frac{\mu_{r,i}^{\text{obs}}}{\sigma_{r,i}^{\text{obs}}}$$

where  $\mu_{r,i}^{\text{obs}}$  and  $\sigma_{r,i}^{\text{obs}}$  are the mean and standard deviation of nearest neighbor distances for cell type  $i$  in the observed ROI  $r$ , respectively. To generate a sample random distribution, we permuted the labels of the RGC type within each ROI  $n = 2000$  times, and repeated the neighbor distance calculation. The NNRI for the null distribution for a given type and ROI was then calculated as above. Note that for SACs, the null distribution was generated by shuffling labels with the other ACs. Additionally, we removed pairs where the # of cell type  $< 20$  ( $\sim 5\%$  of all pairs) as they are too sparse for analysis.

A  $p$  value for each pair is calculated as

$$p_{r,i} = 1 - \text{percentile}\left(\text{NNRI}_{r,i}^{\text{obs}}, P_{r,i}^{\text{null}}\right)$$

Where  $\text{percentile}(x, P_{r,i}^{\text{null}})$  is the percentile value  $x$  is in the distribution  $P_{r,i}^{\text{null}}$ , the null distribution created by the permutation test for cell type  $i$  in roi  $r$ . To generate a single  $p$  value  $p_i$  for a type across ROIs, they are aggregated using Fisher’s method as implemented in `scipy.stats`:

$$p_i = \Pr\left(X_{2R}^2 > -2 \sum_{r=1}^R \ln(p_{r,i})\right)$$

Where  $X_{2R}^2$  is a chi-squared random variable with  $2R$  degrees of freedom. Finally,  $p$  values are adjusted using the Benjamini-Hochberg procedure.

Finally, we note that classical approaches to calculating null NNRI<sup>31</sup> values involve placing somas of finite size and a given density in a blank ROI, followed by the calculation of regularity indices. Our approach, which instead permutes the RGC type labels to generate a null, differs from this because it also respects internal exclusion areas (IEAs), such as blood vessels, the locations of amacrine and non-neuronal cells, and “holes” that arise during the sectioning process. Additionally, our simulation procedure, by design, also takes into account finite soma size and frequency for each simulated type. It is worth noting that our average null NNRI values are around 1.9, which is lower than those calculated in past studies using finite soma size simulations.<sup>31</sup> This is likely due to the presence of IEAs and the inherent constraint that randomization positions are limited to the existing cell positions. Past work suggests that the presence of IEAs and boundary effects<sup>31</sup> can depress calculated regularity indices (also observed in this work), making absolute comparisons of these regularity indices across these studies challenging. Finally, as mentioned earlier, we report only results for RGC types with sufficient cell counts for reliable statistics.

### Data acquisition and quantification for retinal immunohistochemistry data

Confocal imaging was performed using both sexes of mice. Age-matched mice were chosen for comparisons across different genetic labeling. The images were acquired using Zeiss LSM900 (Carl Zeiss Microscopy). Given the avascular regions and uneven flat mounting, imaging and quantification areas were chosen to avoid the retina’s periphery and the optic nerve head. Image acquisitions and quantifications were carried out in a double-blind manner with two researchers.

1. To quantify the distance from immunolabelled RGCs to the nearest vessels, images of retinal flatmounts labeling RGCs (Hoxd10-GFP RGCs, Hb9-GFP RGCs, F-RGCs, and Opn4-tdTomato) were taken using a Zeiss LSM900 microscope with a 20x objective lens with Z-stacks from the superficial layer vessels to the middle layer vessels. Distance measurement in ImageJ was used to measure the shortest surface distance from fluorescently labeled RGCs or RBPMS<sup>+</sup> cells to retinal vessels, as marked by CD31. The shortest distance between the RGC and the blood vessel surfaces. Distances were placed into bins of 1 μm, starting from 0–1 μm, up to 25 μm. RGCs within the 0–1 μm bin were defined as close contact. Comparisons between the cumulative distributions of perivascular distances of RGC types were analyzed using the Anderson-Darling test with the Benjamini-Hochberg multiple testing correction. Within one RGC type, comparisons across replicates were assessed using the K-sample Anderson-Darling test.
2. To count the contacts between human OPN4, BNC2, or FOXP2-positive RGCs and CD31 (PECAM1)<sup>+</sup> blood vessels, we scored by the physical contact based on a 320 μm<sup>2</sup> fluorescent ISH image set taken by Zeiss LSM900 for consistency.
3. To quantify the RGC survival under control conditions or subject to ONC or ND SOHU treatment, we followed an established method for retina wholomount and subsequent quantification methods.<sup>26</sup> After ONC or ND SOHU treatment, images were acquired using 20X magnification on a Zeiss LSM900. The survival rate was calculated as the percentage of RBPMS<sup>+</sup> cells in ONC or ND SOHU eyes compared to eyes that were not treated. Retina images were acquired from at least 8 individual sections using 20X magnification. IMARIS was used to generate cell volumes after background subtraction, and the number of RBPMS<sup>+</sup> cells was counted. Comparisons between the control and the 2 weeks post-crush (2wpc) ONC time point or 3 weeks post-injection (3wpi) were analyzed using One-way ANOVA with Dunnett's multiple comparisons test.

### Statistical methods

Statistical methods and the number of animals tested for each configuration are documented in the figure legends for each experiment. When comparing two groups, statistics were derived using an unpaired two-sided Student's t test or Fisher's exact test, as indicated in the figure legends. One-way analysis of variance (ANOVA) was performed in GraphPad Prism 10 to assess the statistical significance of the differences between multiple measurements. Statistical significance was defined as \* $p < 0.05$ , \*\* $p < 0.01$ , \*\*\* $p < 0.001$ , and \*\*\*\* $p < 0.0001$ .